THE UNIVERSITY OF EDINBURGH

MSc in Theoretical Physics

Multimodal Spin Based Quantum Sensors

Conner J Adlington

Supervisor: Professor Cristian Bonato

August 23, 2024

Abstract

Spin based sensing, particularly with silicon carbide is a growing and exciting field. A great deal of work has gone into developing complex sensing regimes to enable the detection of the magnetic and electric fields, strain, pressure and temperature with nanoscale sensors. This work provides a detailed overview of how that sensing is achieved across both $S = 1$ and $S = 3/2$ systems, particularly with reference to colour centres in Silicon Carbide. Whilst sensing in one mode i.e. detecting one parameter in isolation is well understood, borrowing a lot from the work done with the Diamond Nitrogen vacancy, there is not a great deal of work on where these devices may be used to simultaneously measure multiple parameters. Multimodal sensors could have applications ranging from the laboratory to space and life sciences. We first provide a detailed account of methods already used for single mode sensing. Each schema is given a clear summary which describes the limitations of its implementation. We then attempt to combine the schemas to see which are compatible. We propose four possible combinations of modes and suggest how future work may resolve at least two more combinations. This research thus allows for the implementation of the multimodal techniques by combining existing techniques and may help to direct future research to further develop the field of multimodal sensing.

Declaration

I declare that this dissertation was composed entirely by myself. Chapter 2 gives a detailed overview of the science and does not contain original research. Chapter 3 covers the application of the science outlined in the previous chapter and is primarily a collection of already established techniques. For both Chapter 2 and Chapter 3 many of the calculations were made independently and verified by comparison to literature to ensure the consistency of this work. Chapter 4 is entirely my own work and represents the approaches which warranted inclusion in this work. Many more attempts at combining schemas were made, but were unsuccessful and cannot be concisely included in this work. Finally, Chapter 5 summarises the work completed, discusses wider scientific context and possible directions for future.

Computer modelling was done using Python where specifically the NumPy, MatPlotLib (Pyplot) and SymPy packages were used to numerically diagonalise and plot Hamiltonians and simulate ODMR spectra. Tikz figures at the start of Chapter 2 are adapted from `tikz.net`. All other figures, except where clearly stated, are my own work.

Personal Statement

The project began with developing a deeper understanding of the physics underlying spintronics. The focus was on electron paramagnetic resonance (EPR), specifically using the continuous wave optically detected magnetic resonance technique (CW-ODMR). For this, there is a wealth of literature on the diamond nitrogen vacancy (DNV). Most popular is the application of the DNV as a very sensitive magnetometer.

I worked to understand the intricacies of the diamond systems, with the intention of applying this knowledge to SiC. When I felt comfortable with the underlying physics, I began modelling the different system Hamiltonians. I applied varying $\vec{B}$ and $\vec{E}$ as well as varied temperature. The goal was both to understand the influence of these external factors on the spin-system energy levels as well as to verify my model behaved correctly in the simple cases when compared to existing literature.

When I had the capability to dynamically model both the DNV and several SiC defects, with different spin numbers, I created ensembles of specifically chosen defects to visualise how the CW-ODMR spectra might change under the influence of varying $\vec{B}$, $\vec{E}$ and T. This, as well as existing literature allowed me to isolate specific defects which were most appropriate for the sensing of specific variables. For example, the V2 Silicon defect in SiC is very insensitive to changes in temperature so would not be the most appropriate for thermometry application.

When an ensemble of defects was selected for a specific multi-modal application and the nature of the changes to the ODMR spectra was understood, I worked to develop a method to extract and disentangle the influence of each individual influence on the spectra.

This process was repeated for several model systems and in the end I developed multimodal sensing techniques for specifically chosen defects and external parameters in SiC. In some cases the freedom of the parameters was scoped (i.e. fixing a field direction), however as discussed in the analysis, this still provides value.

Routinely, I met with my supervisor weekly where we would discuss progress and decide on the best way to move the project forwards.

I began writing this dissertation in early-July, determined to give a solid overview of the field. From early August I was working on the write-up full-time.

I consider the project a success but I was frustrated that many of my attempts to disentangle the effects were unsuccessful. Despite this, I thoroughly enjoyed the project and only wish I had more time to keep developing my understanding.

Acknowledgements

I'd like to thank my supervisor **Professor Cristian Bonato** for making this project possible, I am particularly grateful for his patience and his ability to make complex subjects seem approachable and achievable.

I would also like to thank the Royal Air Force **Director of Defence Studies** and the **Chief of the Air Staff** for supporting my completion of this research and I look forward to applying what I have learned to my time in service.

Most of all I would like to thank my wife **Sophie** for her ongoing support and patience. I could not have completed this work without your help.

Contents

5   Conclusions   50

List of Figures

x

Chapter 1

Introduction

Solid-state colour centres, which exists in many materials such as diamond and silicon carbide, have been one of the leading systems in quantum technology [1, 2]. The nitrogen-vacancy (NV) centre in diamond is the most comprehensively studied solid-state spin defect. The defect spin state can be initialized by laser and controlled by microwave [3, 4, 5]. It has been used in various quantum technologies, such spin–photon entanglement, a quantum computing qubit register and high-sensitivity nanoscale quantum sensing, the focus of this work [6, 7].

The NV centre is favoured for it's for its excellent quantum properties, but drawbacks of the system are a lack of established nanotechnology and the fluorescence wavelength of the NV centre, which is in the visible range and limits its wider applications [8, 9, 10]

The field of spectroscopy studies the way atoms and molecules interact with and exchange energy with a wider physical system - specifically through electromagnetic radiation. The electric field interacts with with the electric dipole moment and the magnetic field interacts with a magnetic dipole moment. Magnetic resonance spectroscopy focusses specifically on the interaction between the $\vec{B}$ field with magnetic moments which exist in a given material. This can be broken into two distinct fields:

Nuclear Magnetic Resonance (NMR) which studies the interaction with nuclear magnetic moments.

Electron Paramagnetic Resonance (EPR) which studies the interaction with electron spin systems.

Using Planck's relationship $E = h\nu$ and $c = \lambda\nu$ we may characterise the electromagnetic radiation by its energy which is, to a constant, equivalent to the frequency or the wavelength. We see this resonance in systems where the electrons are influenced by an driving magnetic field forcing transitions between spin system energy levels. In general the measurable difference in energy levels for which the transition occurs is caused by an external magnetic field via the

Zeeman effect. Depending on the symmetry of the spin system, some also exhibit energy level splitting with no applied magnetic field so called zero field splitting (ZFS).

EPR is thus a tool to manipulate electron spins in solid state materials. The transition between energy levels is quantised thus the discrete amount of energy which is lost by the system is transferred into a photon which may be detected optically [11].

A particularly successful technique is optically detected magnetic resonance (ODMR) which uses an applied microwave frequency, an oscillating magnetic field with energy quanta equivalent to the transitions between spin sub-levels, to drive the repopulation of those sub-levels following a spin-preserving radiative transition. In essence this boosts the sensitivity since the microwave driven repopulation induces a change in photoluminescence with a much higher and thus much more readily detectable energy. The techniques of ODMR are so effective that even a single electron spin may be detected this way [12].

Spintronics, a portmantau of **spin** and elec**tronics** is a technology which exploits the characteristics of spin akin to how charge is manipulated in electronics. Fundamentally, the smallest stable magnetic moment available in nature is generated by the spin of a single electron. If efficient read-out can be achieved, the sensitivity of the electron magnetic dipole cannot be matched. Careful construction of an appropriate system, or identification of a system with appropriate characteristics allows for the initialisation, manipulation and read-out of EPR from which we may infer the physical properties of the environment surrounding the system.

With ODMR of the NV centre in diamond the manipulation of individual atomic sized defects at room temperature has been demonstrated [13] despite spin polarisation being a primarily thermodynamic effect (see section 2.14). This is possible since optical excitation of the energy levels decay faster via a spin-preserving transition, leading to a spin polarisation to a in the ground state, provided the system is constantly irradiated for long enough for the system to reach a steady state.

Silicon carbide (SiC) is proving to be an excellent material for application in this space (discussed in detail in section 2.12). A major benefit of SiC is the existence of various polytypes, which each exhibit unique spin colour centre properties. Furthermore, even within a single polytype, these centres can occupy distinct and non-equivalent lattice positions [14]. The existence of these colour centres with similar properties but different energy quanta allows for selection of a specific defect with parameters suitable for the problem at hand.

This work looks to explore how the physical characteristics which influence the Spin Hamiltonian and thus the energy of the electron spin system may be inferred by measuring the effects of those characteristics on the EPR of that system. Further, it will look to explore whether the compound effect of multiple influences may be disentangled and measured simultaneously - so called multi-modal sensing.

Chapter 2 gives a thorough overview of the science behind EPR, SiC, quantum sensing and the

techniques of ODMR. In Chapter 3 we show in detail how different parameters may be sensed using different spin systems. We clearly summarise each approach and list the constraints of each technique. With a clear understanding of what is possible, in Chapter 4 we present the combinations of sensing techniques which may be applied simultaneously - achieving the goal of a multimodal sensing schema. Finally we conclude in Chapter 5 and discuss the implications of the multimodal techniques developed as well as what future work needs to be done to realise other multimodal systems.

Chapter 2

Background

2.1 Magnetism

Where charge ($\vec{E}$-field) has an elementary source unit of a point charge (or monopole) which may be positively or negatively charged. Conversely for magnetism ($\vec{B}$-field) we have the magnetic dipole.

$$\vec{\nabla} \cdot \vec{E} \propto \rho \qquad \qquad \vec{\nabla} \cdot \vec{B} = 0$$
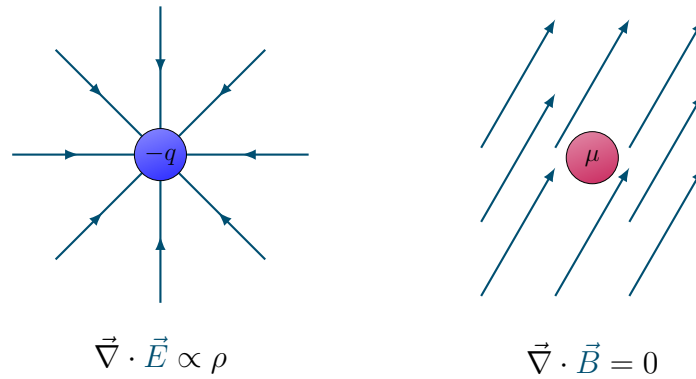
Fig. 2.1: Schematic of electric monopole and magnetic dipole with associated field lines and relevant Maxwell equation.

Magnetic monopoles have never been observed; their existence would also violate Gauss' law ($\vec{\nabla} \cdot \vec{B} = 0$) [15].

2.1.1 Magnetic Dipole

Classically, the magnetic dipole is though of as a loop carrying an electric current (I).

The resultant magnetic dipole moment, $\vec{\mu}$, is defined as the vector at a normal to the plane of the current loop,

$$\vec{\mu} = IS\vec{n} \tag{2.1}$$

where I is the current in, and S the surface area enclosed by, the loop.

The magnetic dipole induces a magnetic field $\vec{B}$, which for points a large distance from the dipole may be calculated as [16]:
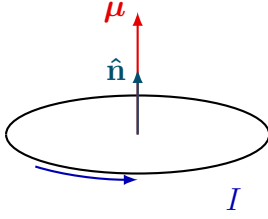
$$\vec{B} = \frac{\mu_0}{4\pi}\frac{1}{r^3}\left[\frac{3(\vec{\mu}\cdot\vec{r})\cdot\vec{r}}{r^2} - \vec{\mu}\right] \qquad (2.2)$$

Fig. 2.2: Schematic of current loop and induced magnetic moment.

The symmetry of the field enables us to consider the direction of the dipole as aligned to the z-axis. Then, defining x, y as usual by $r\cos\theta$ and $r\sin\theta$ respectively. We may decompose the magnetic field in two separate components, parallel (B_z) and perpendicular (B_x, B_y):

$$B_\parallel = \frac{\mu_0}{r^3}(3\cos^2\theta - 1), \quad B_\perp = \frac{3\mu_0}{r^3}\cos\theta\sin\theta.$$

Where we use the Pythagorean principle to determine the overall magnitude $B = |\vec{B}|$ as

$$B = \sqrt{B_\parallel^2 + B_\perp^2}.$$

2.1.2 Gyromagnetic Ratio

Classical Derivation

The current in (2.1) is directly proportional to the current (i.e. the angular momentum of the charge). Specifically, we note that without angular momentum $\vec{G} = \vec{r} \times \vec{p}$ where $\vec{r}, \vec{p}$ represent the radius and the momentum respectively, the dipole moment would be zero.

Dividing the magnetic dipole moment by the angular momentum we find the **gyromagnetic ratio** [17]

$$\gamma = \frac{\vec{\mu}}{\vec{G}}. \qquad (2.3)$$

Without loss of generality we may consider the most simple case, in which the magnetic dipole moment is aligned with the angular momentum for which we may consider only the magnitudes of the dipole moment and the current (angular momentum)

$$\mu = IS, \quad I = \frac{qv}{2\pi R}, \quad S = \pi R^2 \qquad (2.4)$$

we substitute I and S to find

$$\mu = \frac{qvR}{2} \qquad (2.5)$$

and further, we equate the angular momentum vector, using the model of a planar loop to

$$G = m_q v R \tag{2.6}$$

leaving

$$\gamma = \frac{q}{2m_q}. \tag{2.7}$$

We finally consider that we may represent the, currently arbitrary, charge and mass as a sum of electron charges and masses.

$$\gamma = \frac{q}{2m_q} = \frac{\cancel{N}e}{2\cancel{N}m_e} \implies \gamma = \frac{e}{2m_e} \tag{2.8}$$

We therefore find that the gyromagnetic ratio of the electron depends only on fundamental constants [18].

Extending to Quantum Mechanics

Since the gyromagnetic ratio was calculated considering the motion of dipole in a loop, we may extend this to an electron in an orbit. The fundamental change required to extend the model to quantum mechanics is the treatment of angular momentum which should now be quantised. Thus, we replace our classical approximation of $\vec{G} = \vec{r} \times \vec{p}$ with the equivalent quantum mechanical operator,

Fig. 2.3: Schematic of electron in orbit generating a magnetic moment.

$$\hat{G} = \hbar \hat{L} \tag{2.9}$$

here $\hat{L}$ is the operator representation of the angular momentum.

Noether currents tell us that the angular momentum and total energy are conserved in general in a closed system. We thus consider the time independent Shrödinger equation

$$\hat{H}\Psi_n = E_n \Psi_n \tag{2.10}$$

and choose Ψ_n such that it is an eigenfunction of the Hamiltonian, the total angular momentum squared ($L^2 = L_x^2 + L_y^2 + L_z^2$) and exactly one directional component of the angular momentum which is by convention chosen as L_z.

According to quantum mechanics the projection of L along the (m_L) may take integer values $-L, -L + 1, \ldots, L - 1, L$. Thus, we may describe a given quantum state by the angular mo-

mentum L and it's projection m_L. Thus, using Dirac Notation we write

$$\hat{H}\ket{L, m_L} = E\ket{L, m_L} \tag{2.11}$$

$$\hat{L}^2\ket{L, m_L} = L(L+1)\ket{L, M_L} \tag{2.12}$$

$$\hat{L}_z\ket{L, m_L} = m_L\ket{L, m_L}. \tag{2.13}$$

Thus, the operator which describes the orbital magnetic moment may be written using (2.8), (2.9) as

$$\hat{\vec{\mu}}_L = \gamma\hat{\vec{G}}_L = \gamma\hbar\hat{\vec{L}} = \frac{e\hbar}{2m_e c}\hat{\vec{L}}. \tag{2.14}$$

This leads to a quantity known as the **Bohr Magneton**, μ_B, given by [19]

$$\mu_B = \frac{|e|\hbar}{2m_e c}. \tag{2.15}$$

Using this we may write (2.14) as

$$\hat{\vec{\mu}}_L = -\mu_B\hat{\vec{L}}, \tag{2.16}$$

and we may relate the Bohr magneton and the gyromagnetic ratio for the electron as

$$\gamma = g\mu_B. \tag{2.17}$$

2.1.3 g-factor

The above expression is valid for the orbital electron but may be extended to a more general system by introducing a g-factor. The g-factor is therefore equivalent to a dimensionless gyromagnetic ratio [20], so (2.16) may be written with $g = 1$ as

$$\hat{\vec{\mu}}_L = -g\mu_B\hat{\vec{L}}. \tag{2.18}$$

2.2 Spin

As well as the magnetic moment induced by the electron orbit, the electron has an intrinsic magnetic moment. Classically this could be attributed to angular momentum, hence the magnetic moment of elementary particles is termed spin. For a single electron spin may take the value $\pm 1/2$ since the system has only been observed in two possible states [21]. The angular momenta of spin and orbit have been shown to have the same dimensionality and thus they may be summed. The magnetic moment of the spin may thus be expressed as (2.18) [22] where $g \approx 2.0023$ [23, 24].

In reality the electron is point-like and thus the current loop model is unsuitable. Spin is actually a quantum effect and a consequence of the algebra required to satisfy the Dirac equation of relativistic quantum mechanics. The manifestation of this degree of freedom however has the same dimensionality as $\vec{L}$, allowing us to work with the combination of $\vec{L}$ and $\vec{S}$.

We thus consider the total angular momentum of a system J given by

$$J = L + S \tag{2.19}$$

with $L + S, L + S - 1, \ldots, |L - S|$.

For a given system with two electrons, combining the individual spin angular momenta, total spin angular momentum is the addition of the uncoupled spin operators

$$\hat{S} = \hat{S}_1 + \hat{S}_2 \tag{2.20}$$

The coupling results in the formation of four spin states with spin quantum number $S = 0$ and $S = 1$. The spin quantum number $S = 0$ leads to a multiplicity of $2S + 1 = 1$, a so called singlet state.

Fig. 2.4: Schematic of discrete spin levels.

However, the spin quantum number $S = 1$ results in a multiplicity of $2S + 1 = 3$, known as triplet states [25].

2.3   Zeeman Effect

When no magnetic field is applied to a system, the magnetic dipoles of the orbital electron and spin have no preferred direction. The energy levels for all combinations of L and S (all J) are equivalent.

The application of a magnetic field causes an interaction between the spin-system magnetic moment and that field via the Zeeman interaction. The Zeeman effect consists of atomic energy level splitting when an external magnetic field is imposed on a sample [26].

Classically, we calculate the energy of a dipole in a magnetic field as

$$E = -\vec{\mu} \cdot \vec{B} \tag{2.21}$$

may be replaced with the Hamiltonian for a quantum mechanical system

$$\hat{H}_{\text{Zeeman}} = -\hat{\vec{\mu}} \cdot \vec{B}. \tag{2.22}$$

The negative sign is convention used to illustrate that the state of minimum energy is the state

which the moment aligns to the magnetic field.

Thus distinct quantum systems with different J and thus different projections of angular momentum (m_J). This difference in projected angular momentum accounts for the difference in energies between states with differing angular momentum.

Considering $S = 1/2$ system, which has twofold degeneracy, the Zeeman energy is the delta between the spin-system energy with the magnetic moment parallel and anti-parallel to the applied field.
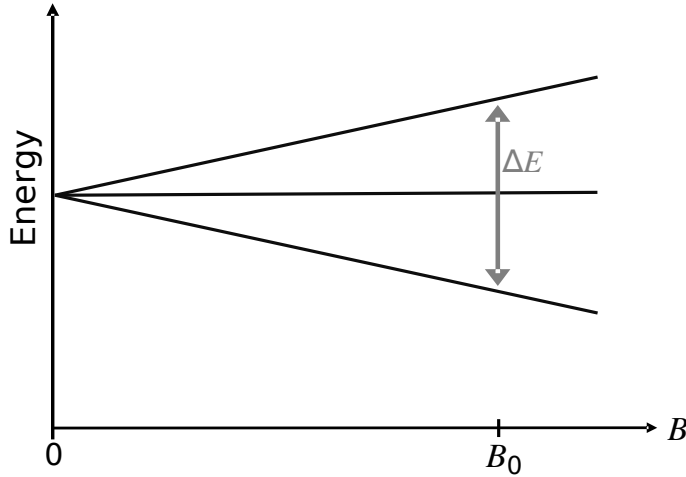
Fig. 2.5: Energy level diagram showing the splitting of the $m_s = 1$ state with applied $\vec{B}$ field. Adapted from figure shown in the work by Grüne.

The Hamiltonian to describe the energy is, using the total angular momentum form of (2.18),

$$\hat{H}_{\text{Zeeman}} = g\mu_B \hat{\vec{S}} \cdot \vec{B}. \tag{2.23}$$

We simplify by aligning the field along the z axis and reduce the scalar product to only the z component. Now for a $S = 1/2$ system i.e. $m_S = \pm 1/2$ we find the Zeeman energy by solving the Shrödinger equation

$$\hat{H}_{\text{Zeeman}} |S, m_S\rangle = E_{\text{Zeeman}} |S, m_S\rangle \tag{2.24}$$

which, to a factor is equivalent to, by (2.13), to

$$\hat{S}_z |S, m_S\rangle = m_S |S, m_S\rangle. \tag{2.25}$$

Thus we find the two eigenvalues to be

$$E_+ = \frac{1}{2}g\mu_B B, \qquad E_- = -\frac{1}{2}g\mu_B B \tag{2.26}$$

and thus the Zeeman energy is given by $g\mu_B B$.

2.4   Spin-Orbit Interaction

The orbital magnetic dipole may interact with the intrinsic spin magnetic dipole via the spin-orbit interaction. This is represented by the spin-orbit Hamiltonian with λ representing the constant of the coupling:

$$H_{\text{SO}} = \lambda \hat{\vec{L}} \cdot \hat{\vec{S}}. \tag{2.27}$$

This is caused by the interaction between the magnetic field induced by the electrons relativistic orbit of the nucleus and its intrinsic spin.

2.5   Perturbation Theory

By considering a ground, non-degenerate state and a perturbation in the electron Zeeman interaction and the spin-orbit coupling we can develop insight into so called zero field splitting. The perturbation is given by

$$\hat{H}' = \hat{H}_{\text{Zeeman}} + \hat{H}_{\text{SO}} \tag{2.28}$$

for which we find

$$E_0 = E_0^{(0)} + \langle 0| \hat{H}' |0\rangle + \sum_n \frac{\langle 0| \hat{H}' |n\rangle \langle n| \hat{H}' |0\rangle}{E_0^{(0)} - E_n^{(0)}}. \tag{2.29}$$

Now, if we consider arbitrary interactions of forms

$$\hat{H}_{\text{Zeeman}} = g_L \mu_B \hat{\vec{L}} \cdot \vec{B} + g_S \mu_B \hat{\vec{S}} \cdot \vec{B} \tag{2.30}$$

$$\hat{H}_{\text{SO}} = \lambda \hat{\vec{L}} \cdot \hat{\vec{S}} \tag{2.31}$$

we may compute the first and second order corrections.

First Order

Substituting (2.30) and (2.31) into (2.29) and integrating only over the orbital values to deduce the Spin Hamiltonian we find

$$\begin{aligned}
\langle 0| \hat{H}' |0\rangle &= \langle 0| g_L \mu_B \hat{\vec{L}} \cdot \vec{B} + g_S \mu_B \hat{\vec{S}} \cdot \vec{B} + \lambda \hat{\vec{L}} \cdot \hat{\vec{S}} |0\rangle \\
&= \langle 0| g_L \mu_B \hat{\vec{L}} \cdot \vec{B} |0\rangle + \langle 0| g_S \mu_B \hat{\vec{S}} \cdot \vec{B} |0\rangle + \langle 0| \lambda \hat{\vec{L}} \cdot \hat{\vec{S}} |0\rangle \\
&= g_L \mu_B \vec{B} \cdot \langle 0| \hat{\vec{L}} |0\rangle + g_S \mu_B \vec{B} \cdot \hat{\vec{S}} \langle 0|0\rangle + \lambda \hat{\vec{S}} \cdot \langle 0| \hat{\vec{L}} |0\rangle \\
&= g_L \mu_B \vec{B} \cdot \langle 0| \hat{\vec{L}} |0\rangle^{\nearrow 0} + g_S \mu_B \vec{B} \cdot \hat{\vec{S}} \langle 0|0\rangle^{\nearrow 1} + \lambda \hat{\vec{S}} \cdot \langle 0| \hat{\vec{L}} |0\rangle^{\nearrow 0} \\
&= g_s \mu_B \hat{S} \cdot \hat{B}.
\end{aligned} \tag{2.32}$$

Here we used the fact that $\langle 0|\hat{\vec{L}}|0\rangle = 0$ since, for example in the alegbraic basis $\hat{L}_z = -i\left(x\frac{\partial}{\partial y} - y\frac{\partial}{\partial x}\right)$ is a Hermitian operator is therefore has eigenvalues which are strictly real numbers, i.e.

$$\hat{L}_z |\psi\rangle = m_L |\psi\rangle. \tag{2.33}$$

By considering (2.33) we see that if we apply an imaginary operator to a real valued eigenfunction the corresponding eigenvalue must be imaginary or zero. We know the state is strictly real since it is non-degenerate[1]. In this case, the expectation value of $\hat{L}$ can only be 0.

Zeeman Splitting.   The result of the first order perturbation is thus a more formal confirmation of the result of section 2.3, specifically (2.26).

Second Order

At second order, again substituting (2.30) and (2.31) into (2.29) and integrating only over the orbital values we find

$$\sum_n \frac{\langle 0|\hat{H}'|n\rangle \langle n|\hat{H}'|0\rangle}{E_0^{(0)} - E_n^{(0)}}$$

$$= \frac{\langle 0|g_L\mu_B\hat{\vec{L}}\cdot\vec{B} + g_S\mu_B\hat{\vec{S}}\cdot\vec{B} + \lambda\hat{\vec{L}}\cdot\hat{\vec{S}}|n\rangle \langle n|g_L\mu_B\hat{\vec{L}}\cdot\vec{B} + g_S\mu_B\hat{\vec{S}}\cdot\vec{B} + \lambda\hat{\vec{L}}\cdot\hat{\vec{S}}|0\rangle}{E_0^{(0)} - E_n^{(0)}}$$

$$= \frac{\langle 0|g_L\mu_B\hat{\vec{L}}\cdot\vec{B} + \lambda\hat{\vec{L}}\cdot\hat{\vec{S}}|n\rangle \langle n|g_L\mu_B\hat{\vec{L}}\cdot\vec{B} + \lambda\hat{\vec{L}}\cdot\hat{\vec{S}}|0\rangle}{E_0^{(0)} - E_n^{(0)}} \tag{2.34}$$

$$= (g_L\mu_B\vec{B} + \lambda\hat{\vec{S}})\underbrace{\sum_n \frac{\langle 0|\hat{\vec{L}}|n\rangle \langle n|\hat{\vec{L}}|0\rangle}{E_0^{(0)} - E_n^{(0)}}}_{\Lambda}(g_L\mu_B\vec{B} + \lambda\hat{\vec{S}})$$

Here Λ is a matrix composed of the elements as shown. Expanding out, this allows us to write the second order perturbation as

$$\sum_n \frac{\langle 0|\hat{H}'|n\rangle \langle n|\hat{H}'|0\rangle}{E_0^{(0)} - E_n^{(0)}} = g_L^2\mu_B^2\vec{B}\cdot\Lambda\cdot\vec{B} + 2\lambda g_L\mu_B\hat{\vec{S}}\cdot\Lambda\cdot\vec{B} + \lambda^2\hat{\vec{S}}\cdot\Lambda\cdot\hat{\vec{S}}. \tag{2.35}$$

Since for EPR we are only interested in the spin-dependent terms, the first term may be neglected as it represents a global shift in the energy spectra.

---

[1]A complex wavefunction ψ is at least doubly degenerate; the complex conjugate ψ^* has the same energy.

Combined Perturbation

Combining (2.32) and (2.35) we find

$$\langle 0|\,\hat{H}'\,|0\rangle + \sum_n \frac{\langle 0|\,\hat{H}'\,|n\rangle\,\langle n|\,\hat{H}'\,|0\rangle}{E_0^{(0)} - E_n^{(0)}} = g_S\mu_B\hat{\vec{S}}\cdot\vec{B} + 2\lambda g_L\mu_B\hat{\vec{S}}\cdot\Lambda\cdot\vec{B} + \lambda^2\hat{\vec{S}}\cdot\Lambda\cdot\hat{\vec{S}}$$

$$= \mu_B\hat{\vec{S}}\cdot\underbrace{(g_S + 2g_L\lambda\Lambda)}_{g}\cdot\vec{B} + \hat{\vec{S}}\cdot\underbrace{\lambda^2\Lambda}_{D}\cdot\hat{\vec{S}}. \tag{2.36}$$

In this expression g and D are matrix quantities depending on Λ and represent the (possibly anisotropic) g factor and D the fine structure splitting.

In this work we consider g to be isotropic and constant, thus g is reduced to a scalar quantity in the spin Hamiltonian.

The term depending on D has no dependence on magnetic field and thus this fine-structure splitting is known as zero field splitting (ZFS) and is observed in systems with $S > 1/2$.

$$H_{\mathrm{FS}} = \hat{\vec{S}}\cdot D\cdot\hat{\vec{S}}. \tag{2.37}$$

2.6 Zero Field Splitting

ZFS is in fact due to the combined effects of fine structure and a dipole-dipole interaction. These effects manifest themselves identically which makes them difficult to separate experimentally. They each depend on a traceless matrix D, as will be shown, which can be totally described by two parameters, conventionally labelled D and E. For simplicity in this work we will consider the combined effect of both the fine-structure and the dipole-dipole interaction as the ZFS interaction. This means when D and E are measured for a specific system, they represent the compound effect of fine-structure splitting and the dipole interaction, but totally describe the zero-field splitting.
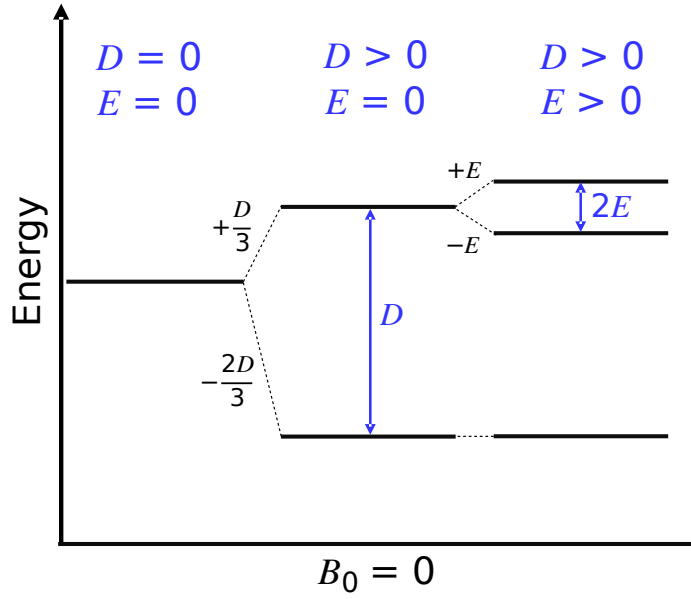
Fig. 2.6: Energy level diagram showing the effect of the zero field splitting parameters D and E in zero magnetic field. Adapted from figure shown in the work by Grüne.

2.6.1   Fine Structure

The matrix D in (2.37) has form

$$D = \begin{pmatrix} D_{xx} & D_{xy} & D_{xz} \\ D_{yx} & D_{yy} & D_{yz} \\ D_{zx} & D_{zy} & D_{zz} \end{pmatrix} \tag{2.38}$$

which may be simplified by alignment to the wider system axis and diagonalising the matrix as

$$D = \begin{pmatrix} D_{xx} & 0 & 0 \\ 0 & D_{yy} & 0 \\ 0 & 0 & D_{zz} \end{pmatrix}. \tag{2.39}$$

The trace of the matrix $\text{Tr}(D)$ is unchanged by the change of basis. Since for EPR we are only concerned with the changes in energy and not the absolute, we may choose the value of the trace without any loss of generality, so we set it equal to zero.

$$\text{Tr}(D) = 0. \tag{2.40}$$

This means that the diagonal form of D may be fully determined by just two parameters

$$D = D_{zz} - (D_{xx} + D_{yy})/2 \tag{2.41}$$

$$E = (D_{xx} - D_{yy})/2 \tag{2.42}$$

Here D represents the axially symmetric parameter and E represents any non-axial contribution of the fine-structure interaction.

Substituting (2.41) and (2.42) into (2.37) and expanding allows us to write our fine-structure Hamiltonian as

$$H_{\mathrm{FS}} = D\left(\hat{S}_z^2 - \frac{1}{3}S(S+1)\right) + E\left(\hat{S}_x^2 - \hat{S}_y^2\right). \tag{2.43}$$

2.6.2 Dipole-Dipole Interaction

We will now show that the interaction of the spin of two electrons has the same form as (2.37) by considering two electrons ($S = 1/2$).

Classically, the energy between two magnetic dipoles, μ_1, μ_2 is calculated as

$$E = \frac{1}{r^3}\left(\mu_1 \cdot \mu_2 - \frac{3(\mu_1 \cdot \vec{r})(\mu_2 \cdot \vec{r})}{r^2}\right). \tag{2.44}$$

To uplift the classical expression to quantum mechanics, we substitute the operator representations for the spin induced dipoles

$$H_{\mathrm{DD}} = g_S^2 \mu_B^2 \frac{1}{r^3}\left(\hat{\vec{S}}_1 \cdot \hat{\vec{S}}_2 - \frac{3(\hat{\vec{S}}_1 \cdot \vec{r})(\hat{\vec{S}}_2 \cdot \vec{r})}{r^2}\right). \tag{2.45}$$

Considering the total spin of the system we may expand this to obtain [11]

$$H_{\mathrm{DD}} = \frac{1}{2r^5} g_S^2 \mu_B^2 \hat{\vec{S}} \cdot \underbrace{\begin{pmatrix} r^2 - 3x^2 & -3xy & -3xz \\ -3xy & r^2 - 3y^2 & -3yz \\ -3xz & -3yz & r^2 - 3z^2 \end{pmatrix}}_{D} \cdot \hat{\vec{S}}. \tag{2.46}$$

As with (2.39) the matrix D in (2.46) has a constant trace (which we may select to be 0) leaving the form of the dipole-dipole interaction identical to that of the fine structure interaction

$$H_{\mathrm{DD}} = \hat{\vec{S}} \cdot D \cdot \hat{\vec{S}}. \tag{2.47}$$

We therefore decompose the traceless matrix D into the axial and non-axial parameters D and

E as above.

2.6.3   Zero Field Splitting Hamiltonian

Determining D and E by experiment will yield the combined effect will be contained within those measurements so we may therefore describe the zero field splitting interaction as a whole using

$$H_{\mathrm{ZFS}} = D\left(\hat{S}_z^2 - \frac{1}{3}S(S+1) \right) + E\left(\hat{S}_x^2 - \hat{S}_y^2 \right). \tag{2.48}$$

The effects of D and E on a triplet state are illustrated in Figure 2.6.

2.7   Nuclear Hamiltonians

There are three additional contributions to the Hamiltonian to be considered which involve an interaction with the nucleus.

2.7.1   Nuclear Zeeman

Equivalent to electron Zeeman interaction but for the nuclear magnetic moment.

$$H_{\mathrm{Zeeman\,(n)}} = -g_n \mu_n \vec{B} \cdot \hat{\vec{I}} \tag{2.49}$$

It is clear that this contribution is not spin-dependent, therefore it will manifest as a global energy shift and is not of interest for EPR. For this reason, the nuclear Zeeman interaction contribution will not be included for the remainder of this work.

2.7.2   Nuclear Quadrupole

Equivalent to the electron dipole-dipole but for nuclear magnetic moments.

$$H_{\mathrm{Quadrupole}} = \hat{\vec{I}} \cdot Q \cdot \hat{\vec{I}} \tag{2.50}$$

As for the nuclear Zeeman interaction, this contribution is not spin-dependent and the contribution will not be included for the remainder of this work.

2.7.3   Hyperfine Interaction

Equivalent to Fine Structure (ZFS) but between the nuclear and electron moment.

$$H_{\text{Hyperfine}} = \hat{\vec{S}} \cdot A \cdot \hat{\vec{I}} \tag{2.51}$$

$$H_{\text{Hyperfine}} = A_{\parallel} \hat{S}_z \hat{I}_z + A_{\perp} (\hat{S}_y \hat{I}_y + \hat{S}_z \hat{I}_z) \tag{2.52}$$

For the systems discussed in this work, hyperfine couplings are usually too small to detect, thus manifest as inhomogeneous line broadening [27]. We therefore do not include the hyperfine contribution for the remainder of this work.
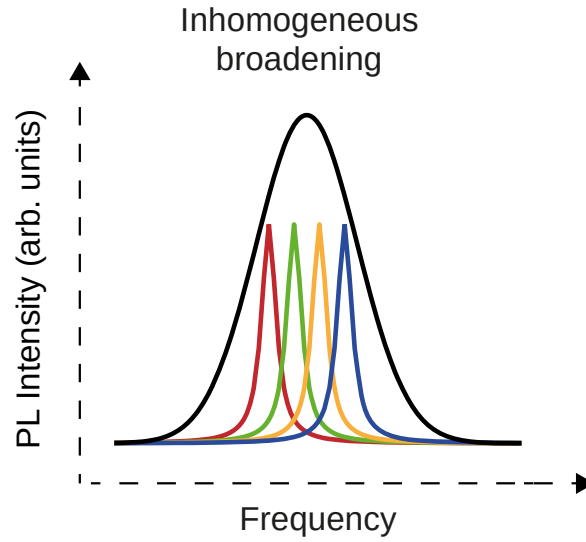
Fig. 2.7: Illustration of the inhomogeneous line broadening caused by the hyperfine interactions. The individual resonances sum to a broader, brighter peak reproduced from Rainò et al.

2.8   Stark Effect

For our Spin Hamiltonian given by

$$H = H_{\text{ZFS}} + H_{\text{Zeeman}} + H_{\text{Hyperfine}} + H_{\text{Zeeman (n)}} + H_{\text{Quadrupole}}$$
$$H = \hat{\vec{S}} \cdot \vec{D} \cdot \hat{\vec{S}} + g\mu_b \hat{\vec{S}} \cdot \vec{B} + \hat{\vec{S}} \cdot A \cdot \hat{\vec{I}} - \mu_n g_n \hat{\vec{I}} \cdot \vec{B} + \hat{\vec{I}} \cdot Q \cdot \hat{\vec{I}}. \tag{2.53}$$

In the most general sense, an applied electrical field could change any of the parameters. We will disregard the effect of the electrical field on the nuclear Zeeman term as the nucleus is paramagnetically shielded [28]. Therefore, we add the contributions of an applied electrical field $\vec{E}$

as $H + H_{\text{Stark}}$ where

$$H_{\text{Stark}} = \vec{E} \cdot \left(\hat{\vec{S}} \cdot R \cdot \hat{\vec{S}} + T\mu_B \hat{\vec{S}} \cdot \vec{B} + \hat{\vec{S}} \cdot F \cdot \hat{\vec{I}} + \hat{\vec{I}} \cdot q \cdot \hat{\vec{I}} \right). \tag{2.54}$$

Here R, T, F, q are matrices for each component of the electric field given by

$$R_{ijk} = \frac{\partial D_{jk}}{\partial E_i}, \quad T_{ijk} = \frac{\partial g_{jk}}{\partial E_i}, \quad F_{ijk} = \frac{\partial A_{jk}}{\partial E_i}, \quad q_{ijk} = \frac{\partial Q_{jk}}{\partial E_i}. \tag{2.55}$$

We may immediately simplify T as for this work we assume isotropic and constant g, for which T is zero.

Further, as discussed in section 2.7 we will not include the contributions of the nuclear Hamiltonians.

This allows us to then consider only the energy change due to the shift in the D parameter (R), which is a square matrix for each component of the applied $\vec{E}$. Exactly as we did for ZFS in section 2.6, we may reduce each of these symmetric matrices to a traceless form.

Consider the expansion of $\hat{\vec{S}} \cdot R \cdot \hat{\vec{S}}$ which we calculate explicitly

$$\begin{aligned}
\hat{\vec{S}} \cdot R \cdot \hat{\vec{S}} &= \begin{pmatrix} \hat{S}_x & \hat{S}_y & \hat{S}_z \end{pmatrix} \cdot \begin{pmatrix} R_{xx} & R_{xy} & R_{xz} \\ R_{xy} & R_{yy} & R_{yz} \\ R_{xz} & R_{yz} & R_{zz} \end{pmatrix} \cdot \begin{pmatrix} \hat{S}_x \\ \hat{S}_y \\ \hat{S}_z \end{pmatrix} \\
&= R_{xx}\hat{S}_x^2 + R_{yy}\hat{S}_y^2 + R_{zz}\hat{S}_z^2 \\
&\quad + R_{xy}(\hat{S}_x\hat{S}_y + \hat{S}_y\hat{S}_x) + R_{xz}(\hat{S}_x\hat{S}_z + \hat{S}_z\hat{S}_x) + R_{yz}(\hat{S}_y\hat{S}_z + \hat{S}_z\hat{S}_y).
\end{aligned} \tag{2.56}$$

We set the constant trace equal to zero and rewrite

$$R_{xx}\hat{S}_x^2 + R_{yy}\hat{S}_y^2 + R_{zz}\hat{S}_z^2 = R_D \left(\hat{S}_z^2 - \frac{1}{3}S(S+1) \right) + R_E \left(\hat{S}_x^2 - \hat{S}_y^2 \right). \tag{2.57}$$

Where R_D and R_E are defined in terms of R the same way D and E are in terms of D, see (2.41), (2.42).

Then, we may write H_{Stark} in this basis as

$$\begin{aligned}
H_{\text{Stark}} = \vec{E} \cdot \Bigg(& R_D \left(\hat{S}_z^2 - \frac{1}{3}S(S+1) \right) + R_E \left(\hat{S}_x^2 - \hat{S}_y^2 \right) \\
& + R_{xy}(\hat{S}_x\hat{S}_y + \hat{S}_y\hat{S}_x) + R_{xz}(\hat{S}_x\hat{S}_z + \hat{S}_z\hat{S}_x) + R_{yz}(\hat{S}_y\hat{S}_z + \hat{S}_z\hat{S}_y) \Bigg).
\end{aligned} \tag{2.58}$$

The final step is to reduce the number of coefficients by exploiting the symmetry of the system. We will study systems with the point group symmetry of C_{3v} [29] which reduces the Hamiltonian

again to [28]

$$H_{\text{Stark}} = R_{113} \left(E_x(\hat{S}_x\hat{S}_y + \hat{S}_z\hat{S}_x) + E_y(\hat{S}_y\hat{S}_z + \hat{S}_z\hat{S}_y) \right)$$
$$- R_{2E} \left(E_x(\hat{S}_x\hat{S}_y + \hat{S}_y\hat{S}_x) + E_y(\hat{S}_x^2 - \hat{S}_y^2) \right) \qquad (2.59)$$
$$+ R_{3D}E_z \left(\hat{S}_z^2 - \frac{1}{3}S(S+1) \right)$$

The coefficient R_{113} represents a mixing of the $m_S = 0$ and $m_S = \pm 1$ states which have an energy splitting of $\mathcal{O}(10^9)$ Hz. The Stark energies are $\sim \mathcal{O}(10^3)$ Hz and of at least second order, thus may be ignored [30].

Thus finally, we write our Stark Hamiltonian as

$$H_{\text{Stark}} = d_{\parallel}E_z \left(\hat{S}_z^2 - \frac{1}{3}S(S+1) \right) - d_{\perp}E_y(\hat{S}_x^2 - \hat{S}_y^2) + d_{\perp}E_x(\hat{S}_x\hat{S}_y + \hat{S}_y\hat{S}_x) \qquad (2.60)$$

where we have labelled the axial contribution as $d_{\parallel}$ and the off-axis contribution as $d_{\perp}$ to match the convention of existing literature.

By direct comparison to (2.48) it is easy to see the first two terms of (2.60) will contribute to the effective ZFS.
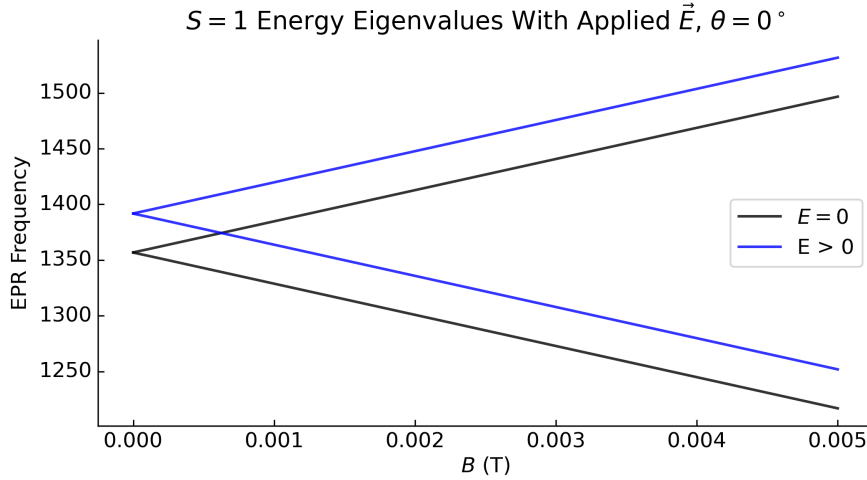
Fig. 2.8: Eigenvalue plot showing the shift of all energy levels when $\vec{E}$ is applied parallel to the defect axis.

In general an electric fields applied along the defect axis has the effect of changing ZFS D which manifests as a shift of all EPR frequencies, shown in figure 2.8. Fields applied perpendicular to the defect axis change E, which either splits (for systems with intrinsic $E = 0$) or amplifies the split (for systems with $E > 0$) of the EPR frequency into two frequencies. The splitting is proportional to the applied field [31, 32], shown in figure 2.9. This allows the parameters $d_{\perp}$ and $d_{\parallel}$ to be measured experimentally.
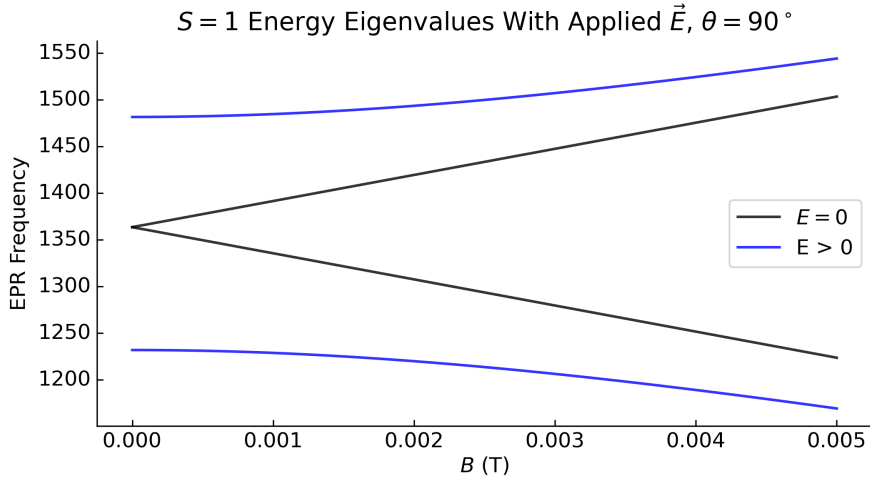
Fig. 2.9: Eigenvalue plot showing the splitting of energy levels when $\vec{E}$ is applied perpendicular to the defect axis.

2.9   Total Hamiltonian

We now have all the components of our total Hamiltonian for both $S = 1$ and $S = 3/2$ systems given by

$$H = H_{\text{Zeeman}} + H_{\text{ZFS}} + H_{\text{Stark}} \tag{2.61}$$

using

$$H_{\text{Zeeman}} = g\mu_B \hat{\vec{S}} \cdot \vec{B}, \tag{2.23}$$

$$H_{\text{ZFS}} = D\left(\hat{S}_z^2 - \frac{1}{3}S(S+1)\right) + E(\hat{S}_x^2 - \hat{S}_y^2), \tag{2.48}$$

and

$$H_{\text{Stark}} = d_\parallel E_z\left(\hat{S}_z^2 - \frac{1}{3}S(S+1)\right) - d_\perp E_y(\hat{S}_x^2 - \hat{S}_y^2) + d_\perp E_x(\hat{S}_x\hat{S}_y + \hat{S}_y\hat{S}_x). \tag{2.60}$$

2.10   Spin Hamiltonian

We can apply (2.61) to our specific $S = 1$ or $S = 3/2$ system by substitution of the spin operators. They are a matrix representation of the $su(2)$ algebra, equivalent to Pauli matrices in the relevant dimension.

2.10.1 $S = 1$ Spin Operators

The three dimensional $S = 1$ spin operators S_j in matrix representation are

$$S_x = \frac{1}{\sqrt{2}}\begin{pmatrix} 0 & 1 & 0 \\ 1 & 0 & 1 \\ 0 & 1 & 0 \end{pmatrix}, S_y = \frac{i}{\sqrt{2}}\begin{pmatrix} 0 & -1 & 0 \\ 1 & 0 & -1 \\ 0 & 1 & 0 \end{pmatrix}, S_z = \frac{1}{\sqrt{2}}\begin{pmatrix} 1 & 0 & 0 \\ 0 & 0 & 0 \\ 0 & 0 & -1 \end{pmatrix}. \qquad (2.62)$$

2.10.2 $S = 3/2$ Spin Operators

The four dimensional $S = 3/2$ spin operators S_j in matrix representation are

$$S_x = \frac{1}{2}\begin{pmatrix} 0 & \sqrt{3} & 0 & 0 \\ \sqrt{3} & 0 & 2 & 0 \\ 0 & 2 & 0 & \sqrt{3} \\ 0 & 0 & \sqrt{3} & 0 \end{pmatrix}, \qquad\qquad S_y = \frac{1}{2i}\begin{pmatrix} 0 & \sqrt{3} & 0 & 0 \\ -\sqrt{3} & 0 & 2 & 0 \\ 0 & -2 & 0 & \sqrt{3} \\ 0 & 0 & -\sqrt{3} & 0 \end{pmatrix},$$

$$S_z = \frac{1}{2}\begin{pmatrix} 3 & 0 & 0 & 0 \\ 0 & 1 & 0 & 0 \\ 0 & 0 & -1 & 0 \\ 0 & 0 & 0 & -3 \end{pmatrix}.$$

$$(2.63)$$

2.11 Other Factors

There are other factors which are known to have an effect on the total energy of the spin system. Those which are understood enough to be applied to sensing are listed.

2.11.1 Temperature

For SiC divacancies ($S = 1$) the ZFS parameter E shows no dependence on temperature. However, the ZFS parameter D varies with temperature.

D has been measured for both the PL5 and PL6 defects in SiC from close to 0K to around 550K and the dependence of D has been fitted to the change in temperature. Both defects show an approximately linear relationship near room temperature which is shown in Figure 2.10.
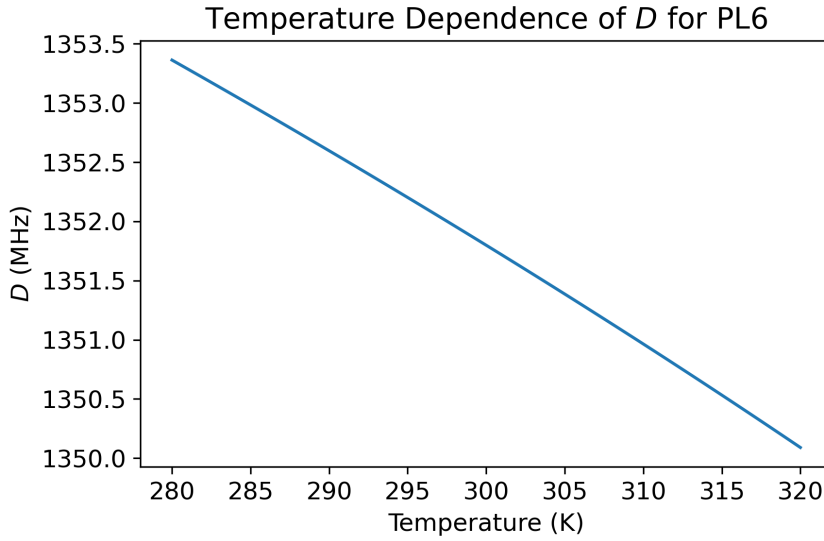
Fig. 2.10: ZFS parameter D temperature dependence for the PL6 $S = 1$ defect from 280K to 320K showing a near linear dependence.

This allows for the consideration of the system temperature, enabling sensing at a range of temperatures. Additionally, if other parameters are well known, the system may be used as a thermometer.

2.11.2 Strain

Strain, which alters the D and E parameters due to a distribution in the ligand field [33] will influence the Hamiltonian. Using the same reasoning as in section 2.8, we could derive a strain Hamiltonian which is identical to (2.60). Therefore, exactly as we consider the "whole effect" of the contributions to the zero field Hamiltonian, we consider the combined effect of strain and applied $\vec{E}$. Put simply, strain is treated as an effective electric field [34].

An application of this duality, is that we may use $\vec{E}$ measuring techniques in shielded environment to determine strain.

2.11.3 Pressure

The effect of pressure has been studied for both SiC divacancies and Silicon vacancies.

In both, the zero field splitting parameter D shows a linear dependence. For this divacancies this has been measured up to 40 GPa [35], for this Silicon vacancy this has been measured up to 27 GPa [36]; both are shown in figure 2.11.
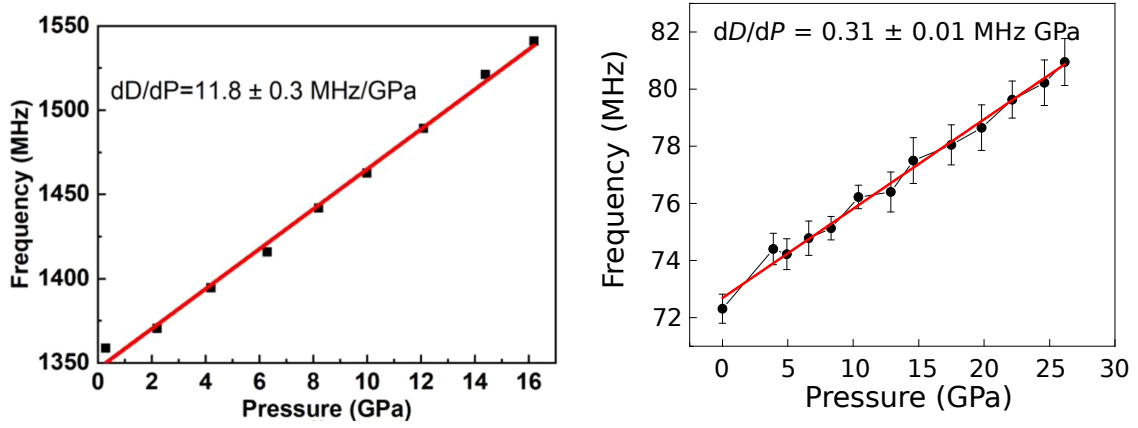
Fig. 2.11: Linear dependence of zero field parameter D to applied pressure for the PL6 divacancy (left) as shown in the work by Liu et al and the Silicon vacancy (right) as shown in the work by Wang et al.

This allows for the consideration of the pressure applied to the system which allows for sensing in environments above ambient pressure. Additionally, if other parameters are held constant or the sensor is designed such that they cannot contribute (e.g. electro-magnetic shielding) the system can be utilised as a pressure gauge.

2.12   Silicon Carbide

SiC is a semiconductor which can be used for high-power and high temperature electronics [37, 38]. Many studies have demonstrated SiC's potential as a host material for qubits, which enables the application of SiC quantum sensors even in ambient conditions [39]. Moreover, the robustness of SiC allows for operation in extreme conditions [40] .

2.12.1   Colour Defects in SiC

Point defects in wide-bandgap semiconductors can have both ground and excited states within the energy gap and, hence, are luminescent centres i.e. colour centres and the luminescence is often stable even at room temperature. Many color centers also possess a non-zero electron spin and can be excellent candidates for optical spin qubits [41].

Multiple colour centres have been observed in SiC, those which may be employed as spin qubits are the divacancy and the Silicon vacancy. There are seven types of divacancies in 4H-SiC, the polytype of SiC for which this work will be based. The defects can be categorised by their orientation within the lattice. These are the c-axis, for which we have the Silicon vacancy V2 and

divacancies PL1, PL2, and PL6. On the basal axis, we have the divacancies PL3, PL4, PL5, and PL7 [42]. Due to having the highest ODMR contrast and coherence at room temperature this work will focus primarily on the c-axis PL6 divacancy and the V2 Silicon vacancy. Application of both of these families of defects in quantum sensing can be competitive with the Nitrogen vacancy in diamond [43].

Figure 2.12 shows the position of the defects in the lattice.
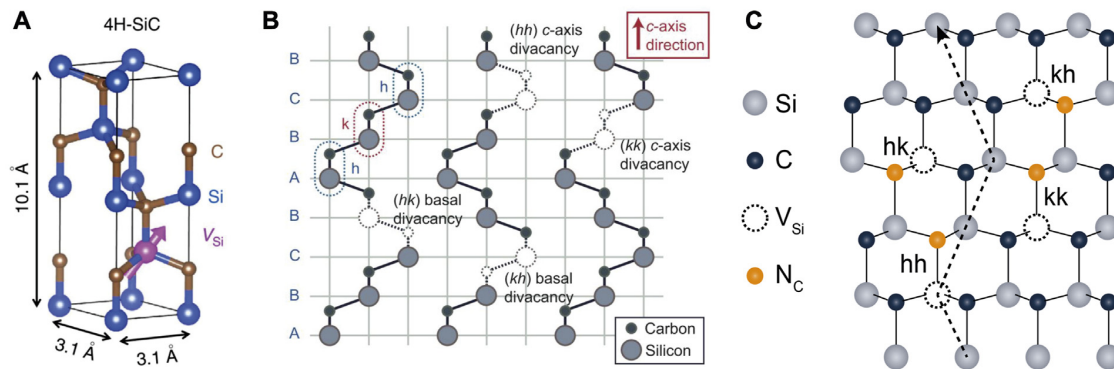
Fig. 2.12: (a) Schematic of the 4H-SiC lattice. (b) Possible non-equivalent divacancies sites within the lattice. (c) Schematic of Silicon vacancies within the lattice. Reproduced from Luo et al.

2.12.2 Production of SiC

Whilst the research for the Nitrogen vacancy in diamond is more mature, many equivalent techniques are being developed for SiC.

Diamond is expensive and not compatible with conventional electronic circuits. By comparison, SiC is a technology-friendly material with an existing large-scale production capacity complemented by mature doping techniques [44]. Wafer-scale SiC is able to be produced and efficiently manufactured into electronic devices down to the atomic scale [45].

Divacancies and Silicon vacancies may reliably introduced into SiC. As an example, the Silicon vacancy can be incorporated into the lattice and the density of the vacancies may be controlled down to the single defect level without degradation of the electrical characteristics of the material [46, 47, 48] .

Further, approaches to manufacture solid-immersion lenses, which may aid the sensitivity or reduce the integration volume of a sensor have been demonstrated [49] .

Overall, research into the applicability of SiC as a quantum sensor is exciting and shows a lot of potential for application in the near term.

2.13   Quantum Sensing

Quantum sensing involves using a qubit system acting as a quantum sensor that interacts with an external variable of interest, such as a magnetic field, electric field, strain or acoustic wave, or temperature [50].

Quantum sensors have a higher sensitivity within a nanoscale volume compared to a fully classical counterpart which would require higher field densities or higher volume interrogation to be effective. They detect such weak signals by exploiting quantum coherence or quantum entanglement [51] . For this work we will study spins states which acquire phase shifts from interactions with specific parameters which may be detected via an optical interface (see 2.15) through spin to photon conversion [52] .

2.13.1   Qubits

A qubit system is, in the simplest terms, a two-level system. The power of a qubit over a conventional bit lies in quantum coherence and/or temporal superposition of quantum states which allow for computation or manipulation with no classical analogue before a collapse back to a measurement basis.

2.13.2   DiVincenzo Criteria

To construct a working quantum sensor with any candidate system, DiVincenzo and Degen outlined a set of four necessary conditions that must be followed [53, 54, 55]. The three which are required for quantum computation, with an added criteria for the ability to efficiently read-out the final state.

1. The quantum system must have discrete resolvable energy levels (or an ensemble of two-level systems with a lower energy state $|0\rangle$ and an upper energy state $|1\rangle$) that are separated by a finite transition energy.

2. It must be possible to initialise the quantum sensor into a well-known state and to read out its state.

3. The quantum sensor can be coherently manipulated, typically by time-dependent fields.

4. The resultant state of the quantum system may be efficiently read-out.

The colour centres in SiC satisfy the first criteria; divacancies and Silicon vacancy are $S = 1$ and $S = 3/2$ spin systems respectively.

Within the context of this work, intitialisation is described in 2.14. We discuss in detail how the spin states are coherently manipulated by the influence of external fields and how the effect of the influence may be measured using ODMR.

2.14 Spin Polarisation

Spin polarisation in the context of EPR is the unequal population of possible spin states. Ordinarily the population of each spin sub-level is governed by Boltzman statistics, thus above cryogenic temperatures, there is no preferential spin sub-level.

For a two-level system at temperature T, statistical mechanics tells us that the probability to be in state $|i\rangle$ is given by

$$p(|i\rangle) = \frac{e^{E_i/k_B T}}{e^{E_0/k_B T} + e^{E_0/k_B T}}. \tag{2.64}$$

If we then consider a two level system $S = 1/2$ under the influence of the Zeeman effect (2.3), the difference in energy is $\Delta E = \gamma B$. Using (2.64) we find

$$p(|+\rangle) = \frac{e^{\gamma B/2k_B T}}{e^{\gamma B/2k_B T} + e^{-\gamma B/2k_B T}} = \frac{1}{1 + e^{-\gamma B/2k_B T}}. \tag{2.65}$$

It is easy to see from (2.65) for room temperature, the probability is around 50%.

We define the polarisation as the normalised difference between the probability of population of two states as

$$P = \frac{p(|+\rangle) - p(|-\rangle)}{p(|+\rangle) + p(|-\rangle)}. \tag{2.66}$$

Substituting (2.64) for our two level system, we see that even in strong magnetic fields the spin states remain unpolarised even when temperature is as low as a few K. However, when we approach $\mathcal{O}(10^{-3})$ K we see polarisation approach 100% with as little as 0.1 T applied [56].

Despite this, it is possible to induce a spin polarisation above cryogenic temperatures and one technique to achieve this is optical polarisation.

2.14.1 Optical Polarisation

For the systems described in this work, optical polarisation is achieved via a Stokes excitation, moving the electron from the ground state to an excited state [57]. This will naturally decay either via a spin preserving transition (which will emit a photon) or a non-spin preserving transition which in general do not emit a photon in the measured frequency range and are referred to as dark states.

These dark decay routes will preferentially reduce the electron to the $m_s = 0$ ground state and
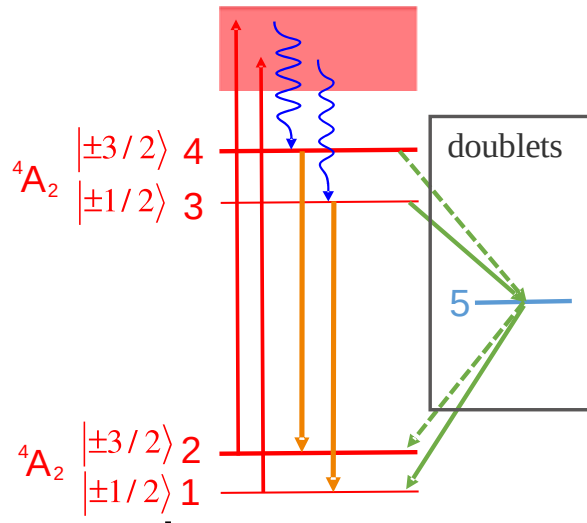
Fig. 2.13: Energy level diagram for a $S = 3/2$ system showing Stokes excitation (red), spin-preseving radiative decay (orange), dark decay routes (green) where the solid arrow is a stronger transition and phonon related decay (blue). Adapted from Wang et al.

on average take a lot longer than the spin preserving transitions.

Polarisation is achieved in the steady state when the defect is illuminated for several excitation/decay cycles. A simple description with reference to figure 2.13 is:

1. The laser is incident on the defect (red arrows) and fast, spin preserving, radiative decays occur taking $m_s = \pm1/2$ excited states to $m_s = \pm1/2$ ground states (and similar for $m_s = \pm3/2$).

2. A proportion of the electrons decay via the non-spin-preserving dark routes (green arrows), for which the solid arrow occurs most often.

3. Since the solid green arrow is preferred, over several cycles, most of the electrons end up decaying to the $m_s = \pm1/2$ ground state, where they will be "stuck" in the much faster, spin preserving cycle. Any dark decay, will return the electron to the $m_s = \pm1/2$

4. The result is a system within which most of the electrons are in the $m_S = \pm1/2$ state.

The process above is a simplification of the actual process but qualitatively describes the process. Optical polarisaion has been demonstrated in SiC and shown to achieve $99 \pm 1\%$ polarisation which is equivalent to reducing the temperature to 5μK [58] .

2.14.2 Rabi Oscillations

From a polarised state, the unequal population of the spin sub-levels is brought back to equilibrium either by the thermodynamic effect (a return to the Boltzman distribution) or by an induced magnetic resonance transition, known as a Rabi oscillation. The Rabi oscillation is what is exploited in EPR and produces a detectable change in photoluminescence in the ODMR spectra.

A driving magnetic field is applied to the system to induce a transition between the $m_s = \pm1/2$ and the $m_s = \pm3/2$ sub-levels in the ground state. This will disrupt the steady state of the system achieved by point 4 in the list above and force a change in photoluminescence which may be detected.

2.15 ODMR

Optically detected magnetic resonance, specifically continuous wave optically detected magnetic resonance will be the read-out mechanism discussed in this work. This is not necessarily the most sensitive mechanism for any given system, but remains popular due to the very simple implementation.

The process is to measure the photoluminescence of the spin polarised sample whilst sweeping the driving field to find where the Rabi oscillations occur. When the change of photoluminescence is at a peak, the Rabi frequency is exactly the energy difference between the two spin sub-levels. The energy of and energy difference between the spin sub-levels is dependent on the magnetic and electric field, temperature, pressure and strain.
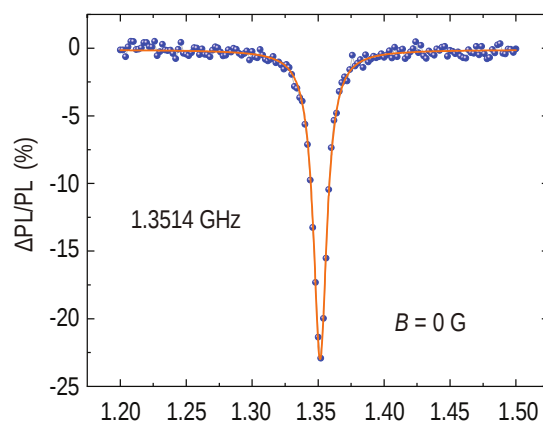
Fig. 2.14: CW-ODMR spectra for a PL6 defect with $\vec{B} = 0$. Blue dots show data from experiment, the orange line is a Lorentzian fit. Adapted from Li et al.

Determination of how these physical characteristics influence the change in ODMR spectra is the topic of this work.

Chapter 3

Design

In this chapter we will provide an overview of how the defects in SiC can be used for magnetometry, thermometry and electrometry in isolation. We will then develop a framework where by combining specific defects we may simultaneously measure multiple parameters.

3.1 $S = 1$ Magnetometry

We will consider the use of a SiC divacancy e.g. PL5 or PL6.

We begin with our total Hamiltonian (2.61). We will consider the system under the influence of only the $\vec{B}$ field, so can remove the Stark effect terms. Additionally, for $S = 1$ we may reduce the constant terms [9] leaving

$$H = g\mu_b \hat{\vec{S}} \cdot \vec{B} + D\hat{S}_z^2 + E(\hat{S}_x^2 - \hat{S}_y^2).$$
(3.1)

By transforming into spherical coordinates, with θ, ϕ the azimuthal and polar angle respectively and $B = |\vec{B}|$

$$
\begin{aligned}
B_x &= g\mu_b B \cos\varphi \sin\theta \\
B_y &= g\mu_b B \sin\varphi \sin\theta \\
B_z &= g\mu_b B \cos\theta
\end{aligned}
$$
(3.2)

then substituting the spin operators (2.62) we find

$$
H = \begin{pmatrix} D + g\mu_b B \cdot \cos\theta & \frac{g\mu_b B}{\sqrt{2}} \cdot e^{-i\cdot\varphi} \cdot \sin\theta & E \\ \frac{g\mu_b B}{\sqrt{2}} \cdot e^{i\cdot\varphi} \cdot \sin\theta & 0 & \frac{g\mu_b B}{\sqrt{2}} e^{-i\cdot\varphi} \cdot \sin\theta \\ E & \frac{g\mu_b B}{\sqrt{2}} \cdot e^{i\cdot\varphi} \cdot \sin\theta & D - g\mu_b B \cdot \cos\theta \end{pmatrix}.
$$
(3.3)

3.1.1 $\vec{B}$ Parallel to Defect

It is straightforward to show from (3.3) that if the magnetic field is applied parallel to the defect axis ($\theta = 0$) then the matrix reduces to

$$H = \begin{pmatrix} D + g\mu_b B & 0 & E \\ 0 & 0 & 0 \\ E & 0 & D - g\mu_b B \end{pmatrix}, \tag{3.4}$$

with eigenvalues

$$E_x = E_y = D \pm \sqrt{(g\mu_b B)^2 + E^2}, \; E_z = 0. \tag{3.5}$$

The uniaxial symmetry of the SiC divacancy means $D \ll E$. Further, we expect to sense in the range where $g\mu_b B \gg D$ therefore we may write the eigenvalues as

$$E_x = E_y \simeq D \pm g\mu_b B, \; E_z = 0. \tag{3.6}$$

That is, for the transitions between $m_s = 0$ and $m_s = \pm 1$[1], the difference is energy reflected in the EPR spectra (visualised in figure 3.1 (right)) is the Zeeman energy

$$\Delta E = 2g\mu_B B = 2\gamma B. \tag{2.26}$$

Representative ODMR Spectra for PL6 ($S = 1$)

$B = 13.4$ mT, $\theta = 60°$

Representative ODMR Spectra for PL6 ($S = 1$)

$B = 6.7$ mT, $\theta = 0°$
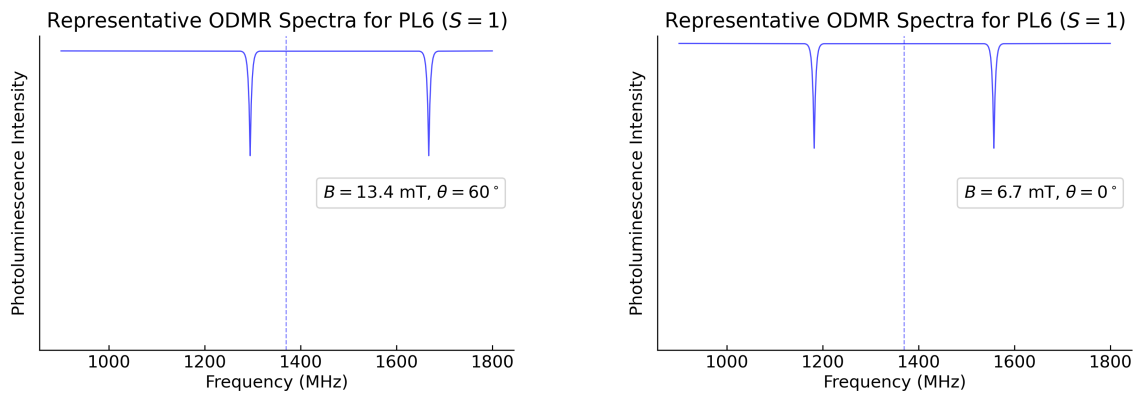
Fig. 3.1: Representative PL6 ODMR spectra showing linear dependence of frequency difference on $B\cos\theta$ and the ZFS shifting of the spectra when $\theta > 0$. Dashed vertical line indicates D.

Thus, for CW-ODMR the difference between the two frequencies $f_1 > f_2$ is directly proportional

---

[1]These are the allowed transitions for optical depopulation due to selection rules. This may be simply thought of as a helicity conservation as the photon is a $S = 1$ particle.

to B

$$f_1 = D + \gamma B, \quad f_2 = D - \gamma B \tag{3.7}$$

It is then straightforward to calculate B using

$$B = \frac{f_1 - f_2}{2\gamma}. \tag{3.8}$$

3.1.2 Vector Magnetometry

By returning to (3.3) it immediately follows from the characteristic equation that eigenvalues λ satisfy

$$0 = \lambda^3 - 2\lambda^2 D + \frac{D(g\mu_b B)^2}{2} + \lambda(D^2 - E^2 - (g\mu_b B)^2) - \frac{1}{2}(g\mu_b B)^2 \underbrace{\left(D\cos(2\theta) - 2E\cos(2\varphi)\sin^2(\theta)\right)}_{\eta} \tag{3.9}$$

where η depends only on the ZFS parameters and the vector of the applied $\vec{B}$ field.

This allows a more general determination of B from the ODMR spectra using

$$B = \frac{\sqrt{\frac{1}{3}\left(f_1^2 - f_1 f_2 + f_2^2 - D^2 - 3E^2\right)}}{g\mu_B}. \tag{3.10}$$

Further we may find η using

$$\eta = \frac{-7D^3 - 4f_1^3 + 6f_1^2 f_2 + 6f_1 f_2^2 - 4f_2^3 + 3D(9E^2 + f_1^2 - f_1 f_2 + f_2^2)}{9(D^2 + 3E^2 - f_1^2 + f_1 f_2 - f_2^2)}. \tag{3.11}$$

Again, exploiting the uniaxial symmetry of our systems we may reduce our expression for η

$$\eta = D\cos(2\theta) - 2E\cos(2\varphi)\sin^2(\theta) \simeq D\cos 2\theta \tag{3.12}$$

therefore with just two frequencies and knowledge of the ZFS parameters, whilst a complete vector cannot be reconstructed, we may determine the magnitude and azimuthal angle of an applied $\vec{B}$ field

$$\theta = \frac{\cos^{-1}(\eta/D)}{2} \tag{3.13}$$

3.1.3 $S = 1$ Magnetometry Summary

We may achieve angle resolved magnetometry using a $S = 1$ system provided:

1. We can resolve **two frequencies** corresponding to the defect in the CW-ODMR spectra.

2. The ZFS parameters D and E are well known.

3. We can determine the magnitude using

$$B = \frac{\sqrt{\frac{1}{3}\left(f_1^2 - f_1 f_2 + f_2^2 - D^2 - 3E^2\right)}}{g\mu_B}. \tag{3.10}$$

4. We can determine the azimuthal angle using

$$\theta = \frac{\cos^{-1}(\eta/D)}{2}. \tag{3.13}$$

3.2 $S = 3/2$ **Magnetometry**

Now we will consider the use of a SiC Silicon vacancy, specifically V2 based on the work by Lee et al [59]. For a general $S = 3/2$ system we begin with (2.61). Again we will only consider the influence of the $\vec{B}$ field leaving

$$H = g\mu_b \hat{\vec{S}} \cdot \vec{B} + D\left(\hat{S}_z^2 - \frac{1}{3}S(S+1)\right) + E(\hat{S}_x^2 - \hat{S}_y^2). \tag{3.14}$$

If the ZFS interaction of the $S = 3/2$ defect is sufficiently strong, the eigenvalues of the spin Hamiltonian show a strong dependence on the orientation of the applied magnetic field.

This induces a non-linear shift of resonance transitions in EPR frequencies, which is seen in the ODMR spectra. Like $S = 1$, this allows information about the applied external magnetic field to be extracted from EPR spectra provided the ZFS parameters are known.

In zero magnetic field the V_{Si} V2 vacancy has an ODMR line maximum ($2D$) around 70 MHz with very weak dependence on temperature.

In order to reconstruct the energy eigenstates we must use the observed resonant energies. There are $2S + 1$ states for a system with spin S from which $2S$ transition frequencies may be found. Therefore, we may find up to three EPR frequencies.

Using the same polar co-ordinate conversion as (3.2) and $B = |\vec{B}|$ we may write the Hamiltio-

nian in matrix form as

$H =$

$$
\begin{pmatrix}
D + \frac{3}{2}g\mu_B B \cdot \cos\theta & \frac{\sqrt{3}}{2}g\mu_B B \cdot \sin\theta \cdot e^{-i\varphi} + \sqrt{3}E & 0 & 0 \\
\frac{\sqrt{3}}{2}g\mu_B B \cdot \sin\theta \cdot e^{i\varphi} + \sqrt{3}E & \frac{1}{2}g\mu_B B \cos\theta - D & g\mu_B B \cdot \sin\theta \cdot \cos\varphi + 2E & 0 \\
0 & g\mu_B B \cdot \sin\theta \cdot \cos\varphi + 2E & -\frac{1}{2}g\mu_B B \cdot \cos\theta - D & \frac{\sqrt{3}}{2}g\mu_B B \cdot \sin\theta \cdot e^{-i\varphi} + \sqrt{3}E \\
0 & 0 & \frac{\sqrt{3}}{2}g\mu_B B \cdot \sin\theta \cdot e^{i\varphi} + \sqrt{3}E & D - \frac{3}{2}g\mu_B B \cdot \cos\theta
\end{pmatrix}.
$$

$$(3.15)$$

3.2.1 $\vec{B}$ Parallel to Defect

Considering B parallel to the defect axis and we find [60] the Hamiltonian reduces to

$$
H = \begin{pmatrix}
D + \frac{3}{2}g\mu_B B & \sqrt{3}E & 0 & 0 \\
\sqrt{3}E & \frac{1}{2}g\mu_B B - D & 2E & 0 \\
0 & 2E & -\frac{1}{2}g\mu_B B - D & \sqrt{3}E \\
0 & 0 & \sqrt{3}E & D - \frac{3}{2}g\mu_B B \cdot
\end{pmatrix}
\tag{3.16}
$$

with eigenvalue equations given by

$$
\lambda = \frac{1}{2}g\mu_B B \pm \sqrt{(D + g\mu_B B)^2 + 3E^2} \text{ or, } \lambda = -\frac{1}{2}g\mu_B B \pm \sqrt{(D - g\mu_B B)^2 + 3E^2}. \tag{3.17}
$$

Which we further simplify for the Silicon vacancy as $E = 0$ [61] to

$$
H = \begin{pmatrix}
D + \frac{3}{2}g\mu_B B & 0 & 0 & 0 \\
0 & \frac{1}{2}g\mu_B B - D & 0 & 0 \\
0 & 0 & -\frac{1}{2}g\mu_B B - D & 0 \\
0 & 0 & 0 & D - \frac{3}{2}g\mu_B B
\end{pmatrix}
\tag{3.18}
$$

which is diagonal so we may immediately read off

$$
\begin{aligned}
\lambda_1 &= & 3/2 g\mu_B B + D \\
\lambda_2 &= & 1/2 g\mu_B B - D \\
\lambda_3 &= - & 1/2 g\mu_B B - D \\
\lambda_4 &= - & 3/2 g\mu_B B + D.
\end{aligned}
\tag{3.19}
$$

3.2.2 Vector Magnetometry

Coming back to (3.15) we find the eigenvalue equation for a general $S = 3/2$ system to be

$$
\lambda^4 - \left(2D^2 + 6E^2 + \frac{5}{2}(g\mu_B B_0)^2 \right) \lambda^2 - 2(g\mu_B B_0)^2 \left(D(3\cos^2\theta - 1) + 3E\sin^2\theta\cos 2\varphi \right) \lambda
$$
$$
+ \frac{9}{16}(g\mu_B B_0)^4 + D^4 - \frac{1}{2}D^2(g\mu_B B_0)^2 - D^2(g\mu_B B_0)^2(3\cos^2\theta - 1) + 3E^2(3E^2 + 2D^2)
$$
$$
+ E(g\mu_B B_0)^2(6D\sin^2\theta\cos 2\varphi + \frac{9}{2}E\cos 2\theta) = 0.
$$
$$(3.20)$$

We may write the general equation for the eigenvalues as

$$
\sum_{n=0}^{2S+1} C_n \lambda^n = 0 \tag{3.21}
$$

we then substitute each eigenvalue λ_i into this general expression to obtain $2S + 1$ equations.

The goal is now to remove all λ_i terms by considering instead the transition frequencies between eigenstates, which are observed in the ODMR spectra. The energy states are not in general sorted with respect to the energy values, so we use the convention that $\lambda_i > \lambda_{i-1}$.

To reduce our number of equations to $2S - 1$ we make the substitutions

$$
\lambda_i + \underbrace{\lambda_{i+1} - \lambda_i}_{f_{i+1,i}} = \lambda_{i+1}, \qquad \lambda_i - \underbrace{(\lambda_i - \lambda_{i-1})}_{f_{i,i-1}} = \lambda_{i-1}
$$

for each $i = 2, \ldots, 2S$ and calculate both

$$
\sum_{n=0}^{2S+1} \frac{C_n \left((\lambda_i + f_{i+1,i})^n - \lambda_i^n \right)}{C_{2S+1}} = 0 \text{ and } \sum_{n=0}^{2S+1} \frac{C_n \left((\lambda_i - f_{i,i-1})^n - \lambda_i^n \right)}{C_{2S+1}} = 0
$$

to find two new simultaneous equations

$$
\sum_{n=0}^{2S} C'_{i,n} \lambda_i^n = 0 \text{ and } \sum_{n=0}^{2S} C''_{i,n} \lambda_i^n = 0.
$$

We may combine these as

$$
\sum_{n=0}^{2S} \frac{C'_{i,n} \lambda_i^n}{C'_{i,2S}} - \frac{C''_{i,n} \lambda_i^n}{C''_{i,2S}} = 0
$$

to obtain an equation for the eigenvalue of the energy eigenstate $|i\rangle$ where $i = 2, \ldots, 2S$:

$$
\sum_{n=0}^{2S-1} C_{i,n}^{(2S-1)} \lambda_i^n = 0. \tag{3.22}
$$

This process is repeated until only one linear equation exists for each eigenvalue, which may be expressed in terms of resonant energies. $f_{i,i-1}$ can then be substituted to find expressions for all other eigenvalues. We obtain equations for λ_2 expressed in terms of $f_{2,1}$, $f_{3,2}$ and λ_3 expressed in terms of $f_{3,2}$, $f_{4,3}$.

Finally, using $f_{3,2} = \lambda_3 - \lambda_2$ we find formulas for each eigenvalues in terms of the resonant frequencies:

$$\lambda_1 = -\frac{3}{4}f_{2,1} - \frac{1}{2}f_{3,2} - \frac{1}{4}f_{4,3} \tag{3.23}$$

$$\lambda_2 = \frac{1}{4}f_{2,1} - \frac{1}{2}f_{3,2} - \frac{1}{4}f_{4,3} \tag{3.24}$$

$$\lambda_3 = \frac{1}{4}f_{2,1} + \frac{1}{2}f_{3,2} - \frac{1}{4}f_{4,3} \tag{3.25}$$

$$\lambda_4 = \frac{1}{4}f_{2,1} + \frac{1}{2}f_{3,2} + \frac{1}{4}f_{4,3}. \tag{3.26}$$

We substitute one of these expressions into one of the equations of the form of equation (3.22) and we obtain

$$5(g\mu_B B)^2 = \left(\frac{\sqrt{3}}{2}f_{4,3} + f_{3,2} + \frac{\sqrt{3}}{2}f_{2,1}\right)^2$$
$$+ (1 - \sqrt{3})(f_{4,3} + f_{2,1})f_{3,2} - f_{4,3}f_{2,1} - 4(D^2 + 3E^2). \tag{3.27}$$

We also find a $S = 3/2$ η which is again useful for angle resolution as it is dependent on the ZFS parameters, θ and φ

$$\eta \equiv E(2\cos^2\varphi\sin^2\theta + \cos^2\theta) + D\cos^2\theta \tag{3.28}$$

which in terms of the resonant frequencies is given by

$$\eta = $$
$$\frac{4\left(8(D + 3E) + 5(f_{4,3} - f_{2,1})\right)(g\mu_B B)^2 + (f_{4,3} - f_{2,1})\left(16(D^2 + 3E^2) - (f_{4,3} - f_{2,1})^2 - 4f_{3,2}^2\right)}{96(g\mu_B B)^2}$$
$$\tag{3.29}$$

where $(g\mu_B B)^2$ may be determined in terms of the frequencies as (3.27).

Overall, this shows that if the ZFS is known and three EPR frequencies are observed, the applied magnetic field strength can be found using (3.27).

Since $E = 0$, $E \ll D$ for the Silicon vacacny, we may approximate η defined in equation (3.28) to

$$\eta \simeq D\cos^2\theta. \tag{3.30}$$

By exploiting this approximation, we can determine the azimuthal angle that the magnetic field vector makes with the defect axis, however at this stage we may not determine anything about the x, y components of the vector.

To do so we explicitly compute η using equation (3.29) then we find the azimuthal angle as

$$\theta = \cos^{-1} \sqrt{\frac{\eta}{D}} \tag{3.31}$$

In a general $S = 3/2$ system, ambiguity is found when computing θ using equation (3.31) as the EPR frequencies can not be mapped to specific transitions.

These ambiguities may be resolved by the application of reference magnetic fields in three orthogonal directions and repeated measurements as described by Niethammer et al [62]. Alternatively, it may be resolved using a technique which exploits a so called magic angle as detailed by Lee et al [59] or by calculating the polar angle based on the ODMR spectra dependent on whether θ is more or less than the magic angle as detailed by Simin et al [47] .

3.2.3 $S = 3/2$ **Magnetometry Summary**

We may achieve angle resolved magnetometry using a $S = 3/2$ system provided:

1. We can resolve **three frequencies** corresponding to the defect in the CW-ODMR spectra.

2. The ZFS parameters D and E are well known.

3. We can determine the magnitude using

$$5(g\mu_B B)^2 = \left(\frac{\sqrt{3}}{2} f_{4,3} + f_{3,2} + \frac{\sqrt{3}}{2} f_{2,1} \right)^2 \\ + (1 - \sqrt{3})(f_{4,3} + f_{2,1})f_{3,2} - f_{4,3}f_{2,1} - 4(D^2 + 3E^2). \tag{3.27}$$

4. We can determine the azimuthal angle using

$$\theta = \cos^{-1} \sqrt{\frac{\eta}{D}} \tag{3.31}$$

3.3 $S = 1$ **Electrometry**

We consider a SiC divacancy and again begin with the total Hamiltonian (2.61). In this case we need all elements of the equation

$$H = g\mu_B \hat{\vec{S}} \cdot \vec{B} + D(\hat{S}_z^2) + E(\hat{S}_x^2 - \hat{S}_y^2)$$
$$+ d_\parallel E_z(\hat{S}_z^2) - d_\perp E_y(\hat{S}_x^2 - \hat{S}_y^2) + d_\perp E_x(\hat{S}_x\hat{S}_y + \hat{S}_y\hat{S}_x).$$

(2.61)

For this discussion we will consider the effective electric field as $\vec{\mathcal{E}} = \vec{E} + \vec{\sigma}$ the sum of both the applied field and that which is induced by the strain. Without loss of generality we may switch the x, y which will help in the simplification.

$$H = \begin{pmatrix} D + d_\parallel \mathcal{E} \cos\theta_E + g\mu_b B \cdot \cos\theta_B & \frac{g\mu_b B}{\sqrt{2}} \cdot e^{-i\cdot\varphi_B} \cdot \sin\theta_B & E - d_\perp \mathcal{E} e^{-i\varphi_E} \sin\theta_E \\ \frac{g\mu_b B}{\sqrt{2}} \cdot e^{i\cdot\varphi_B} \cdot \sin\theta_B & 0 & \frac{g\mu_b B}{\sqrt{2}} e^{-i\cdot\varphi_B} \cdot \sin\theta_B \\ E - d_\perp \mathcal{E} e^{i\varphi_E} \sin\theta_E & \frac{g\mu_b B}{\sqrt{2}} \cdot e^{i\cdot\varphi_B} \cdot \sin\theta_B & D + d_\parallel \mathcal{E} \cos\theta_E - g\mu_b B \cdot \cos\theta_B \end{pmatrix}.$$

(3.32)

It is easy to see that to maximally reduce the contribution of the magnetic field on the diagonal elements, we should orient the magnetic field perpendicular to the defect ($\theta_B = 90°$). Defining $\mathcal{E}_\perp = \sqrt{\mathcal{E}_x^2 + \mathcal{E}_y^2}$ and $B_\perp$ similarly, we find if the $\vec{B}$ field was parallel to the defect axis $\theta = 0$ the Hamiltonian reduces to

$$H = \begin{pmatrix} D + d_\parallel \mathcal{E} \cos\theta_E + g\mu_b B & 0 & E - d_\perp \mathcal{E} e^{-i\varphi_E} \sin\theta_E \\ 0 & 0 & 0 \\ E - d_\perp \mathcal{E} e^{i\varphi_E} \sin\theta_E & 0 & D + d_\parallel \mathcal{E} \cos\theta_E - g\mu_b B \end{pmatrix}.$$

(3.33)

The eigenvalues may be found as for section 3.1 for the $m_s = 0$ to $m_s = \pm 1$ transitions and are

$$f_\pm \simeq D + d_\parallel \mathcal{E}_\parallel \pm \sqrt{(g\mu_B B)^2 + (d_\perp \mathcal{E}_\perp)^2}.$$

(3.34)

Since the parallel component of the field is equivalent to a correction to ZFS D and raises the whole spectra, we find

$$\mathcal{E}_\parallel d_\parallel = \frac{f_1 + f_2}{2} - D.$$

(3.35)

We find a similar expression for the perpendicular component as

$$\mathcal{E}_\perp d_\perp = \sqrt{\frac{1}{4}(f_1 - f_2)^2 - (g\mu_B B)^2}.$$

(3.36)

Clearly this allows us to deduce the azimuthal angle and magnitude as

$$\theta = \tan^{-1}\left(\frac{\mathcal{E}_{\parallel}}{\mathcal{E}_{\perp}}\right), \quad \mathcal{E} = \sqrt{\mathcal{E}_{\perp}^2 + \mathcal{E}_{\parallel}^2}. \tag{3.37}$$

This method is mathematically sound, but the energy difference is suppressed by the parallel $\vec{B}$ field and would require careful alignment of the magnetic field to the defect axis. A general expression for the difference in EPR frequencies for the $m_s = 0$ to $m_s = \pm 1$, $\Delta f_{\pm}$ is [63]

$$\Delta f_{\pm} = d_{\parallel} E_z \pm \left(F(\vec{B}, \vec{E}, \vec{\sigma}) - F(\vec{B}, 0, \vec{\sigma}) \right) \tag{3.38}$$

where

$$F(\vec{B}, \vec{E}, \vec{\sigma}) = \left((\mu_B g B_z)^2 + d_{\perp}^2 \mathcal{E}_{\perp}^2 - \frac{(\mu_B g B_{\perp})^2}{D} d_{\perp}\mathcal{E}_{\perp} \cdot \cos(2\varphi_B + \varphi_{\mathcal{E}}) + \frac{(\mu_B g B_{\perp})^4}{4D^2} \right)^{\frac{1}{2}} \tag{3.39}$$

and

$$F(\vec{B}, 0, \vec{\sigma}) = \left((\mu_B g B_z)^2 + d_{\perp}^2 \sigma_{\perp}^2 - \frac{(\mu_B g B_{\perp})^2}{D} d_{\perp}\sigma_{\perp} \cdot \cos(2\varphi_B + \varphi_{\sigma}) + \frac{(\mu_B g B_{\perp})^4}{4D^2} \right)^{\frac{1}{2}}. \tag{3.40}$$

If $\vec{B}$ is well known, this reduces to a function of E, θ and ϕ which may be approximated using a best fit algorithm up to a four-fold symmetry. This means if $\vec{B}$ is well known, then possibilities for $\vec{E}$ can be calculated. This would leave ambiguity in $\vec{E}$ which could be resolved by the application of known reference fields just as in 3.2.

3.3.1 $S = 1$ Electrometry Summary

We may achieve angle resolved electrometry using a $S = 1$ system provided:

1. The direction and magnitude of $\vec{B}$ and the ZFS parameters D and E are well known.

2. We can resolve **two frequencies** corresponding to the defect in the CW-ODMR spectra.

3. In general, the shift of EPR frequencies due to the applied electric field is given by

$$\Delta f_{\pm} = d_{\parallel} E_z \pm \left(F(\vec{B}, \vec{E}, \vec{\sigma}) - F(\vec{B}, 0, \vec{\sigma}) \right) \tag{3.38}$$

Sensitivity is maximised when $\vec{B}$ is applied perpendicular to the defect axis.

We can determine the vector by fitting θ and φ to Δf eliminating the ambiguity by applying reference fields and repeating measurements.

4. Despite the reduction in sensitivity, applying $\vec{B}$ parallel to the defect axis we may reduce the Hamiltonian to find the magnitude and azimuthal angle as

$$\theta = \tan^{-1}\left(\frac{\mathcal{E}_\parallel}{\mathcal{E}_\perp}\right), \quad \mathcal{E} = \sqrt{\mathcal{E}_\perp^2 + \mathcal{E}_\parallel}. \tag{3.37}$$

3.4 $S = 1$ **Thermometry**

Again for $S = 1$ we will consider a divacancy which have zero- field splitting (ZFS) frequencies are at approximately $D = 1.365$ GHz [64].

For this application we will need every term in (2.61) as D is affected by $\vec{B}$, $\vec{E}$, temperature, and pressure [65]. We will reduce the constant terms as we did in 3.1

$$\begin{aligned} H &= g\mu_B \hat{\vec{S}} \cdot \vec{B} + D(\hat{S}_z^2) + E(\hat{S}_x^2 - \hat{S}_y^2) \\ &+ d_\parallel E_z(\hat{S}_z^2) - d_\perp E_y(\hat{S}_x^2 - \hat{S}_y^2) + d_\perp E_x(\hat{S}_x \hat{S}_y + \hat{S}_y \hat{S}_x). \end{aligned} \tag{2.61}$$

In this discussion we will consider the pressure to be constant, but as we will describe at the end of this section, by holding temperature constant the same scheme could be used to detect pressure.

There are two main approaches to thermometry:

ZFS Temperature Dependence. The ZFS D may, depending on the specific spin system being studies, be sensitive to changes in temperature, which will be exploited in this section.

Photoluminescence. The photoluminescence of the spin system may have a dependence on temperature, which we will exploit in section 3.5.

We will exploit the temperature dependence of ZFS D which results from thermal lattice expansion and a temperature dependence of the electron–phonon interaction [66, 67]. We will also consider the influences of $\vec{B}$ and $\vec{E}$ to be well known, this could be achieved by careful experiment design or by measurement. We will therefore assume they may be disregarded in this discussion with the exception of a well known $\vec{B}$ field applied along the defect axis.

This allows us to reduce our Hamiltonian down to only

$$H' = D(T)\hat{S}_z^2 \tag{3.41}$$

which when we substitute our spin operator (2.62) we find

$$H' = \begin{pmatrix} D(T) & 0 & 0 \\ 0 & 0 & 0 \\ 0 & 0 & D(T) \end{pmatrix}. \tag{3.42}$$

We see from (3.42) that the $m_s = \pm 1$ states are both uniformly affected by the temperature dependence of D while the $m_s = 0$ state is not influenced by the change. Therefore, the $\Delta m_s = \pm 1$ transitions, detectable in EPR, are affected.

The temperature dependence of D is visualised as a magnetic field is applied along the defect axis in figure 3.2.
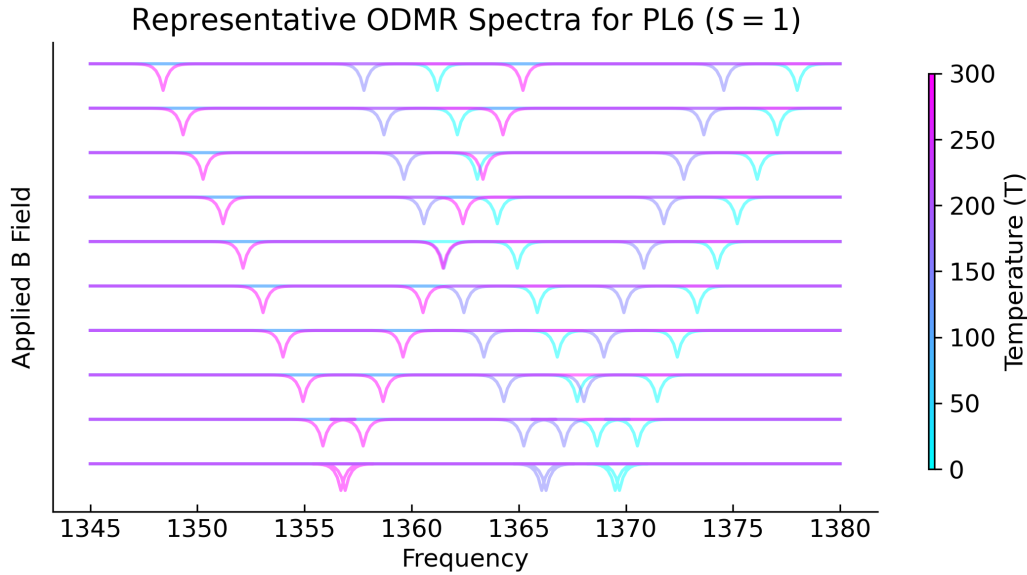
Fig. 3.2: Representative ODMR plot for the PL6 defect at 0K, 150K and 300K showing the dependence of ZFS D on temperature.

For any $B > 0$, since the Zeeman effect acts on the $m_s = \pm 1$ states symmetrically we may find D using

$$f_1 = D(T) + \gamma B, \quad f_2 = D(T) - \gamma B \tag{3.43}$$

and computing $D(T)$

$$D(T) = \frac{f_1 + f_2}{2}. \tag{3.44}$$

The temperature dependence of D has been studied for both PL5 and PL6 [?, ?]. The PL6 dependence may be fit to the Debye-model formula [68], Varshni-form formula [69] or a polynomial-form formula [70, 71]

$$D(T) = 1364.6 + 3.5 \times 10^{-3}T - 1.8 \times 10^{-4}T^2$$
$$- 1.5 \times 10^{-7}T^3 + 1.6 \times 10^{-9}T^4 - 2.710^{-12}T^5 \text{ MHz}.$$
$$(3.45)$$

Any of the fits may be used to infer temperature from the measured value of D.

> ### 3.4.1 $S = 1$ Thermometry Summary
>
> We may achieve thermometry using a $S = 1$ system provided:
>
> 1. The influence of other factors affecting D are well known, $\vec{E}_\parallel$ and pressure.
>
> 2. The temperature dependence of the defect has been studied and fit to an equation e.g.
>
> $$D(T) = 1364.6 + 3.5 \times 10^{-3}T - 1.8 \times 10^{-4}T^2$$
> $$- 1.5 \times 10^{-7}T^3 + 1.6 \times 10^{-9}T^4 - 2.710^{-12}T^5 \text{ MHz}. \qquad (3.45)$$
>
> 3. We can resolve **one frequency** (in zero field) or **two frequencies** if the $m_s = \pm 1$ degeneracy has been lifted corresponding to the defect in the CW-ODMR spectra. This may be used to find D e.g. with $B \parallel z$ we have
>
> $$D(T) = \frac{f_1 + f_2}{2} \qquad (3.44)$$

The methods described in this section have exploited the change of ZFS D due to temperature, which is characteristically the same as the change due to pressure. The scheme may therefore be used for sensing pressure as well as sensing temperature.

3.5 $S = 3/2$ Thermometry

We consider again the V2 Silicon vacancy which due to the 4H-SiC trigonal pyramidal symmetry has a stable ground state ZFS with respect to temperature and can not be used for thermometry [50].

Schemas have been developed which exploit the increase in photoluminescence in the vicinity of level anti-crossings to measure the change in the excited state D as in the work by Anisimov et al.

We will focus instead on an alternative all optical method which exploits the dependence on temperature of the photoluminescence of the spin system.

Anti-Stokes excitation is a process in which the wavelength of the exciting photon is longer (i.e.

lower energy) than that of the emitted photons (visualised in figure 3.4). The mechanisms of anti-stokes excitation have been studied and include multiphoton absorption, phonon absorption, and Auger recombination [72, 48].
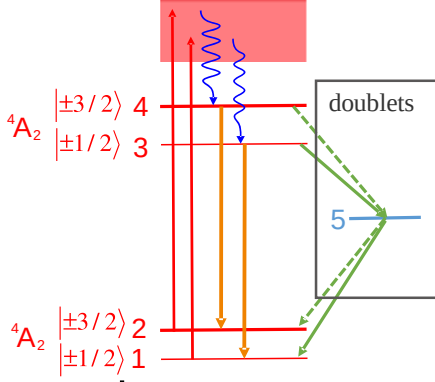
Fig. 3.3: Energy level diagram showing Stokes excitation. Colours as described in figure 2.13. Adapted from Wang et al.

The anti-Stokes excitation process depends on a contribution from phonons (blue arrows in in figure 3.4).

By comparing the intensity of the anti-Stokes and Stokes photoluminescence we find the ratio between the intensities to be proportional to the phonon density, which are determined by a Bose–Einstenin distribution [73]

$$\frac{I_{\mathrm{AS}}}{I_{\mathrm{S}}} \propto \exp\left\{\frac{\Delta E}{k_B T} - 1\right\} \tag{3.46}$$

where I_{AS} and I_{S} represent respectively the intensities of the anti-Stokes and Stokes photoluminescence at a datum laser power. ΔE represents the difference in energy between the incident photon and the zero phonon line i.e. the phonon contribution to the excitation.

We may reduce this to a temperature dependent exponential curve when $\Delta E \ll k_B T$ as (3.46) reduces to

$$\frac{I_{\mathrm{AS}}}{I_{\mathrm{S}}} \propto \exp\left\{\frac{\Delta E}{k_B T}\right\}. \tag{3.47}$$

Wang et al analysed the Silicon vacancy under anti-Stokes excitation [74]. The zero phonon line for the defect is around 917nm, so a Stokes excitation was induces by a laser with $1030 > 917$nm and the anti-Stokes excitation was induced by a laser with $720 < 917$nm. Using the same power for both lasers, the intensity of the photoluminescence from the anti-Stokes excitation increased as temperature increased. Conversely the intensity from the Stokes excitation decreased with temperature. The ratio therefore agrees with the statistical model in (3.46).

Thus to realise a thermometer, we fit data to (3.47) with measurable proportionality and correction factors a, b, c, T_0 as [72]
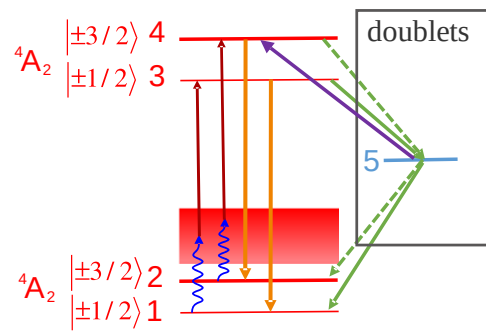
Fig. 3.4: Energy level diagram showing anti-Stokes excitation. Colours as described in figure 2.13. Adapted from Wang et al.

$$\frac{I_{\mathrm{AS}}}{I_{\mathrm{S}}} = a + b \exp\left\{-\frac{c}{T - T_0}\right\}. \tag{3.48}$$

Temperature may then be inferred by solving the equation as

$$T = T_0 - \frac{c}{\ln\left(\left[\frac{I_{\mathrm{AS}}}{I_{\mathrm{S}}} - a\right]/b\right)}. \tag{3.49}$$

For the SiC Silicon vacancy the intensity ratio, and thus the proposed thermometry sensitivity, is most sensitive at room temperature and above.

This technique is also extremely versatile as the influence of external parameters, providing they do not change the position of the zero phonon line (effect ZFS D), does not affect the measurement. For example, figure 3.5 shows that the ODMR signature which can be used to detect magnetic field can be read in parallel to the ratio of intensities of the Stokes/anti-Stokes excitations. We will discuss how this may be applied in Chapter 4.
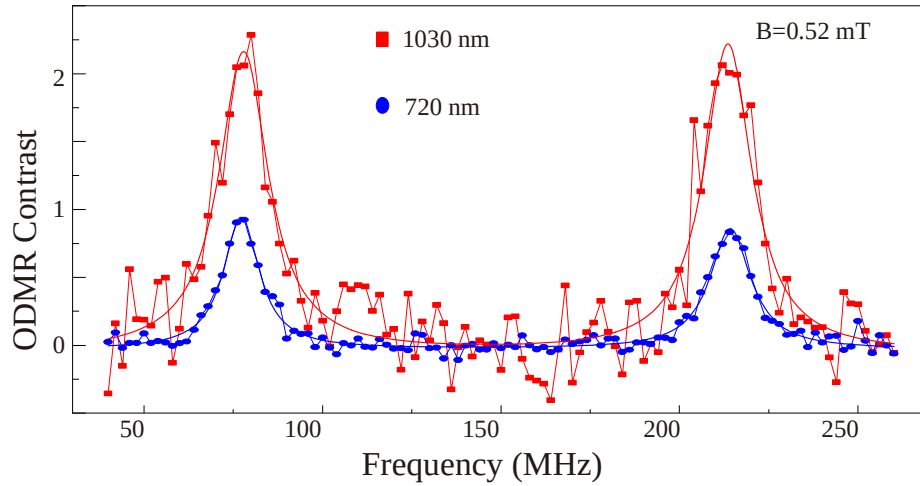
Fig. 3.5: ODMR spectra for V2 Silicon vacancy using Stokes (blue) and anti-Stokes (red) excitation. This shows the Rabi frequencies are the same under either excitation scheme. Adapted from Wang et al

3.5.1 $S = 3/2$ Thermometry Summary

We may achieve optical thermometry using an $S = 3/2$ system provided:

1. The ZFS parameters D and E are well known and we may determine the position of the zero phonon line.

2. The system is responsive to both Stokes and anti-Stokes excitation and the intensities of the subsequent emission can be measured.

3. The temperature dependence of the ratio between intensities has been studied and

mapped to an exponential equation as

$$\frac{I_{\mathrm{AS}}}{I_{\mathrm{S}}} = a + b \exp\left\{-\frac{c}{T - T_0}\right\}, \tag{3.48}$$

from which the temperature can be calculated as

$$T = T_0 - \frac{c}{\ln\left(\left[\frac{I_{\mathrm{AS}}}{I_{\mathrm{S}}} - a\right]/b\right)}. \tag{3.49}$$

Chapter 4

Results and Analysis

4.1 Proposed Systems

We have described schemas for measuring the $\vec{E}$ field, $\vec{B}$ field, temperature, pressure and strain. We will say that the measurement of T and P should be considered equivalent in a $S = 1$ system and the measurement of strain is equivalent to $\vec{E}$ in all systems.

Thus, we have $^4C_2 = 6$ distinct pairwise combinations we may consider for multimodal application: $(\vec{B}, T)$, $(\vec{B}, P)$, $(\vec{B}, \vec{E})$, $(\vec{E}, T)$, $(\vec{E}, P)$ and (T, P).

We will discuss the combinations for which multi-modality is possible using the techniques described in this work. Throughout the discussion, all external parameters not discussed are assumed to be absent.

4.1.1 $\vec{B}$ and Temperature

In general, simultaneously measuring $\vec{B}$ and T is not possible as when the magnetic field is at $\theta \neq 90$, ZFS D may not be inferred from the ODMR spectra. However, aligning $\vec{B}$ perpendicular to the defect axis allows D to be calculated from the spectra and the magnitude of the field to be measured.

> **$|\vec{B}|$ and Temperature Proposal**
>
> We exploit the temperature independence of the V2 Silicon vacancy to measure the $\vec{B}$ field. Temperature may then be measured by either the same defect using anti-Stokes technique or a divacancy where temperature may be inferred from the change in ZFS D.

The implementation is to capture the ODMR spectra of the defects. Figure 4.1 shows a two simulated spectra for a V2 and PL6 ensemble at 250K and 350K (offset for clarity). Clearly the V2 spectra is unaffected by temperature allowing $\vec{B}$ to be measured from the three frequencies as

Fig. 4.1: Representative ODMR spectra for an ensemble of PL6 and V2 defects showing the shift in ZFS D due to temperature in the PL6 and lack of shift in the V2. Dashed lines indicate the position of D for the PL6 defect.

described in summary 3.2.3. Providing the ZFS D of the PL6 is under no other influence e.g. pressure or $\vec{E}_\parallel$, $D(T)$ may be read from the two frequencies of the PL6 defect as described in 3.4.1.

4.1.2 $\vec{B}$ and Pressure

As for 4.1.1 this is not possible in general and required $\vec{B}$ to be perpendicular to the defect axis.

$|\vec{B}|$ and Pressure Proposal

We exploit the linear dependence of the V2 Silicon vacancy D and pressure, and the linear dependence on Δf of the divacancy on the applied $\vec{B}$ field. We determine the pressure from the average of the two EPR frequencies for the divacancy and use the inferred pressure to perform magnetometry.

The approach is slightly less straight forward as the ZFS D of the Silicon vacancy shows a linear dependence on P. Thus, we cannot cleanly separate the two parameters as above. However, since the dependence is linear, as is the dependence of an $S = 1$ defect splitting on the $\vec{B}$ field, and the B field does not influence D, we may still determine the parameters simultaneously.

The implementation is to first measure $D(P)$ by taking the average of the two frequencies of the $S = 1$ defect (3.5.1). Now the pressure is known, calculate $D(P)$ for the Silicon vacancy and perform magnetometry with the V2 Silicon vacancy as detailed in 3.2.3.
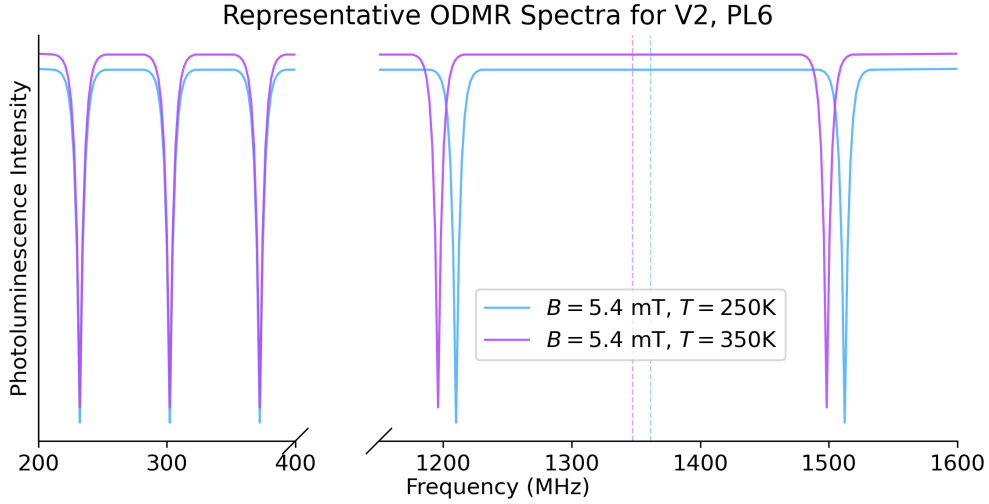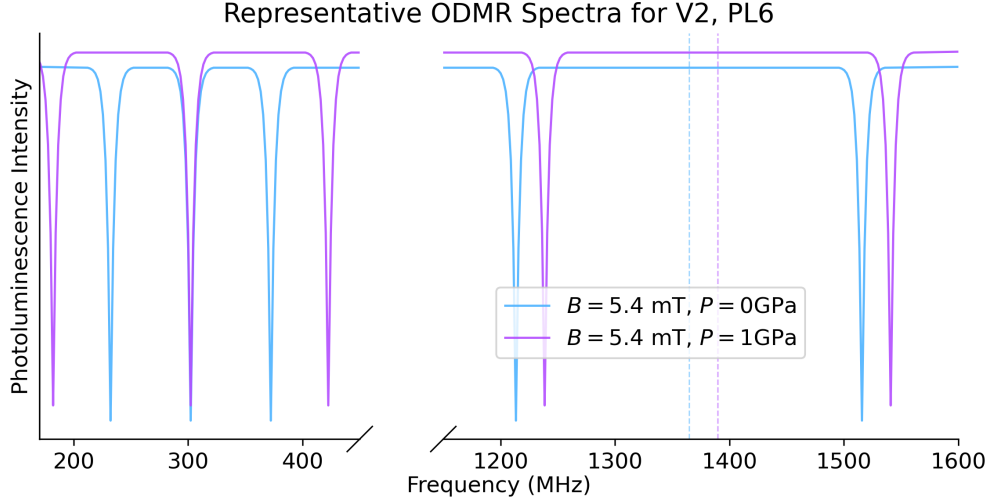
Fig. 4.2: Representative ODMR spectra for an ensemble of PL6 and V2 defects showing the shift in ZFS D of both the PL6 and V2 defect due to applied pressure. Dashed lines indicate the position of D for the PL6 defect.

4.1.3 Temperature and Pressure

Simultaneously measuring temperature and pressure may be achieved using only the V2 Silicon vacancy. Illustrative ODMR plots are shown with $\vec{B}$ applied parallel to the defect axis.

> **Temperature and Pressure Proposal**
>
> The temperature independence of the V2 Silicon vacancy allows the CW-ODMR spectra to be inspected to evaluate P from $D(P)$. With knowledge of the effective D, tune two lasers to a Stokes and anti-Stokes frequency and perform $S = 3/2$ temperature measurements.

The ODMR spectra of the V2 Silicon vacancy in zero field (magnetic or electric) will show a single peak at the effective D. This may be used to determine the position of the zero phonon line from which temperature measurement can be performed as described in 3.5.1.

In practice, readily tuning lasers to respond to the effective D may be impractical. If future work mapped a function $D(P,T)$ for the divacancy, it could be used to perform temperature measurement using only CW-ODMR techniques.

To demonstrate, we (naively) assume the effects of temperature and pressure on the ZFS D of the divacancy linearly combine, we visualise this in figure 4.3.

If all three frequencies are visible ($f_1 < f_2 < f_3$) in the $S = 3/2$ spectra we see using (3.19) that we may determine D using

$$D(P) = \frac{f_1 - f_3}{4},\tag{4.1}$$

from which we infer the pressure P_0 as no dependence on T is shown.
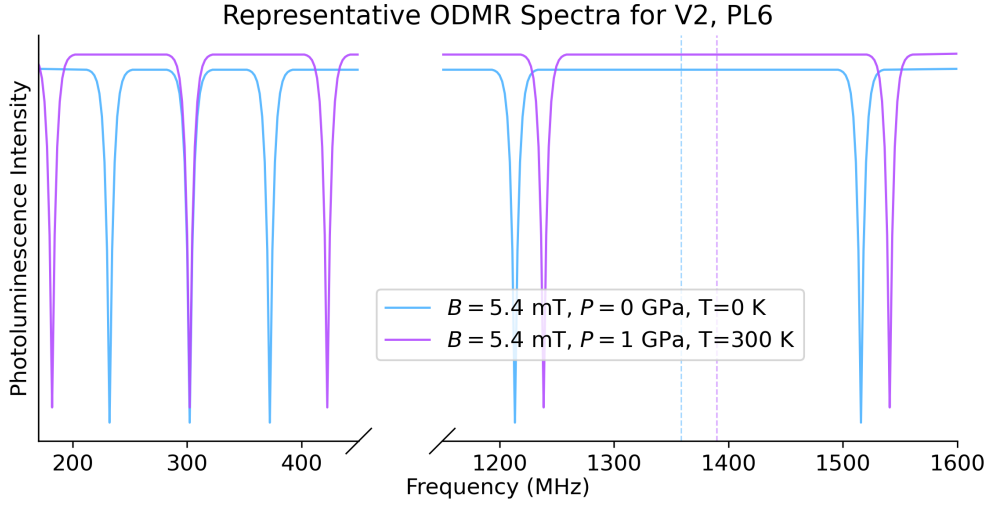
Fig. 4.3: Representative ODMR spectra for an ensemble of PL6 and V2 defects showing the inequivalent shifting of ZFS D due to pressure and temperature assuming the effects compound additively. Dashed lines indicate the position of D for the PL6 defect.

We now fit the data to compute T in the using the divacancy frequencies (ν_1, ν_2) as

$$D(T, P_0) = \frac{\nu_2 + \nu_1}{2}. \tag{4.2}$$

4.1.4 $\vec{E}$ and Temperature or Pressure

The measurement of $\vec{E}$ in parallel to temperature (pressure) is less clear, as the influence of $E_{\parallel}$ is indistinguishable from a change in temperature (pressure) - a net change in ZFS D. Ideally, we would exploit the temperature independence of the V2 defect D but we have been unable to find a schema for $S = 3/2$ electrometry. Thus, within the context of this work we have been unable to find a scheme to simultaneously measure $\vec{E}$ and temperature (pressure) in general.

An exception can be made however if careful alignment of the $\vec{E}$ is possible, then the magnitude may be measured.

> **$|\vec{E}|$ and Temperature (Pressure) Proposal**
>
> The $\vec{E}$ field is aligned perpendicular to the defect axis. Then by (3.36) we may determine the magnitude with no dependence on D. With knowledge of the $|\vec{E}|$, choose a defect on the same axis and calculate the influence of $\vec{E}$ on D and E. Measure $D(\vec{E}, T)$ and fit the data to calculate the temperature (pressure) of the system.

We infer from the electrometry Hamiltonian (3.32) that the corrections to D and E are

$$\Delta D = d_{\parallel} |\vec{E}| \cos \theta_E, \quad \Delta E = d_{\perp} |\vec{E}| \sin \theta_E. \tag{4.3}$$

We exploit that when $\theta = 90°$ the ZFS D is not affected by the field and any variation must be due to temperature (pressure).

In the absence of an applied magnetic field (which would have to of known magnitude and applied parallel to the defect axis for this schema to work), E is determined from the effective magnitude of ZFS E by the difference in the frequencies as

$$E_\perp d_\perp = E_0 - \sqrt{\frac{(f_1 - f_2)^2}{4} - (g\mu_B B)^2}, \tag{4.4}$$

where E_0 is the ZFS E of the defect without influence of the electric field.

Temperature (pressure) sensing can also then be performed using the same two measured frequencies as $D(T)$ will be the average of them.

Figure 4.4 which shows a strictly perpendicular electric field allows a visualisation of the described effects.
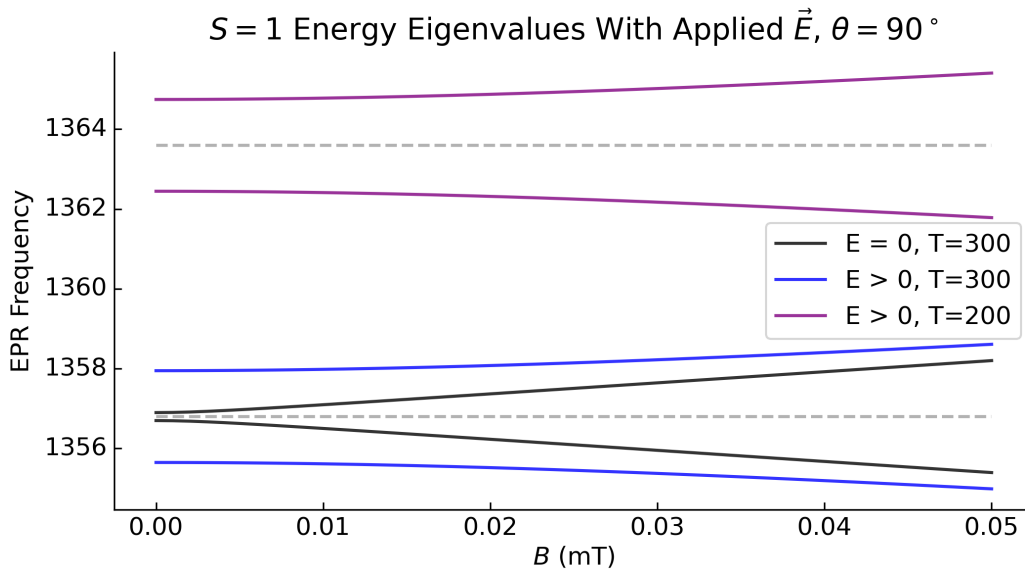
Fig. 4.4: Eigenvalue plot showing that ZFS D (dashed line) is the average of the two measured frequencies at a given temperature, parallel $\vec{B}$ field and perpendicular $\vec{E}$ field.

4.1.5   Trimodal $\vec{B}$, Temperature and Pressure

$\vec{B}$, Temperature and Pressure Proposal

We exploit the temperature independence of the V2 Silicon vacancy to perform a pressure measurement. Then, having fixed P_0, we infer T. Now, since T and P are well known, we may perform scalar magnetometry using either the $S = 1$ or $S = 3/2$ defects provided the magnetic field is aligned parallel to the defect axis.

This method simply extends the method described in 4.1.3. By fixing the orientation of the field, the magnitude of the field may be computed from either the $S = 1$ or $S = 3/2$ spectra respectively as

$$B = \frac{\nu_2 - \nu_1}{2g\mu_B}, \quad B = \frac{f_3 + f_1}{2g\mu_B} = \frac{f_2}{g\mu_B}. \tag{4.5}$$

Chapter 5

Conclusions

Overall, the scope of multimodality which can be achieved depends very heavily on the complex interconnection of the parameter influence. By constraining a freedom of one of the parameters the interplay is significantly simplified and allows more possibility for multimodal measurement. Whilst more restrictive, this is still relevant as many physical systems, for which nanoscale sensors of this kind will be useful, will have predictable characteristics. This is particularly valid as the PL6 and V2 only occupy the c-axis in 4H-SiC meaning comparing the defect axis to the laboratory frame is simplified.

By means of an example, a transistor on a chip will have a direction in which current may flow and the magnetic field will curl around that flow of current. These defects may be implanted (or the system) designed such that the incident field is parallel to the defect axis. Which, if the interplay between temperature and pressure was developed would allow for optical determination of the current across the transistor (inferred from $|\vec{B}|$), temperature and pressure.

For multimodal sensing without constraint, the temperature independence of the ZFS D parameter in the V2 Silicon vacancy showed the most obvious application. Further research into the interplay between temperature and any other characteristic will expand the scope of what it is possible to simultaneously sense. Additionally, any work to investigate the properties of defects in SiC which may identify another defect with a particular insensitivity would enable great development in the multimodal space.

For constrained multimodal sensing, schemas were more readily developed which exploit the reduction in complexity when the off diagonal terms in the Hamiltonian were suppressed. Another area which could aid development would be the design of a $S = 3/2$ $\vec{E}$ field schema. This would allow us to exploit the temperature stable ZFS D in the V2 defect to combine detection of the electric field and temperature.

We showed that if the interplay between T and P and the combined effect on ZFS D could be understood then we may simultaneously measure temperature and pressure and even extend a trimodal sensing.

An approach considered in this work, albeit unsuccessful was to attempt to reduce the ambiguity within some of the systems by comparing the effects on basal and c-axis defects. Similar schemes are used with the Diamond nitrogen vacancy, however that system has four distinct defect orientations and so integration into three dimensional space is overdetermined. Conversely for SiC there are only two distinct orientations and thus integration into three dimensional space is underdetermined. Further, at temperatures above cryogenic, some of the alternative defects produce very low contrast. Thus, in the context of multimodality, even if solved, the technique would likely be inappropriate.

5.1 Wider Scientific Context

Equipped with the methods developed in this work, specific systems may be identified (similar to the transistor example above) where the constrained multimodal schemes could be implemented into already established electronic systems. Further, due to the resilience of SiC and the scale of the proposed sensors the multimodal techniques presented here may also be applied in the laboratory and aid the development of other fields, particularly in harsh environmental conditions. For example, investigating the threshold voltage instability in SiC and monitoring the parameters using already implanted defects.

Overall, this work represents a foot in the door of the possibilities for multimodal spin based quantum sensing and has highlighted clear and specific opportunities for impactful future research.

Bibliography

[1] Nguyen T. Son, Christopher P. Anderson, Alexandre Bourassa, Kevin C. Miao, Charles Babin, Matthias Widmann, Matthias Niethammer, Jawad Ul Hassan, Naoya Morioka, Ivan G. Ivanov, Florian Kaiser, Joerg Wrachtrup, and David D. Awschalom. Developing silicon carbide for quantum spintronics. *Applied Physics Letters*, 116(19), May 2020.

[2] David D. Awschalom, Ronald Hanson, Jörg Wrachtrup, and Brian B. Zhou. Quantum technologies with optically interfaced solid-state spins. *Nature Photonics*, 12(9):516–527, August 2018.

[3] Gang Zhang, Yuan Cheng, Jyh-Pin Chou, and Adam Gali. Material platforms for defect qubits and single-photon emitters. *Applied Physics Reviews*, 7(3), September 2020.

[4] Mete Atatüre, Dirk Englund, Nick Vamivakas, Sang-Yun Lee, and Joerg Wrachtrup. Material platforms for spin-based photonic quantum technologies. *Nature Reviews Materials*, 3(5):38–51, April 2018.

[5] Romana Schirhagl, Kevin Chang, Michael Loretz, and Christian L. Degen. Nitrogen-vacancy centers in diamond: Nanoscale sensors for physics and biology. *Annual Review of Physical Chemistry*, 65(1):83–105, April 2014.

[6] B. Hensen, H. Bernien, A. E. Dréau, A. Reiserer, N. Kalb, M. S. Blok, J. Ruitenberg, R. F. L. Vermeulen, R. N. Schouten, C. Abellán, W. Amaya, V. Pruneri, M. W. Mitchell, M. Markham, D. J. Twitchen, D. Elkouss, S. Wehner, T. H. Taminiau, and R. Hanson. Loophole-free bell inequality violation using electron spins separated by 1.3 kilometres. *Nature*, 526(7575):682–686, October 2015.

[7] C. E. Bradley, J. Randall, M. H. Abobeih, R. C. Berrevoets, M. J. Degen, M. A. Bakker, M. Markham, D. J. Twitchen, and T. H. Taminiau. A ten-qubit solid-state spin register with quantum memory up to one minute. *Phys. Rev. X*, 9:031045, Sep 2019.

[8] William F. Koehl, Bob B. Buckley, F. Joseph Heremans, Greg Calusine, and David D. Awschalom. Room temperature coherent control of defect spin qubits in silicon carbide. *Nature*, 479(7371):84–87, November 2011.

[9] David J. Christle, Abram L. Falk, Paolo Andrich, Paul V. Klimov, Jawad Ul Hassan, Nguyen T. Son, Erik Janzén, Takeshi Ohshima, and David D. Awschalom. Isolated electron spins in silicon carbide with millisecond coherence times. *Nature Materials*, 14(2):160–163, December 2014.

[10] Matthias Widmann, Sang-Yun Lee, Torsten Rendler, Nguyen Tien Son, Helmut Fedder, Seoyoung Paik, Li-Ping Yang, Nan Zhao, Sen Yang, Ian Booker, Andrej Denisenko, Moham-mad Jamali, S. Ali Momenzadeh, Ilja Gerhardt, Takeshi Ohshima, Adam Gali, Erik Janzén, and J¨org Wrachtrup. Coherent control of single spins in silicon carbide at room temper-ature. *Nature Materials*, 14(2):164–168, December 2014.

[11] A. Carrington and A.D. McLachlan. *Introduction to Magnetic Resonance with Applications to Chemistry and Chemical Physics*. A Harper international edition. Harper & Row, 1967.

[12] J. Köhler, J. A. J. M. Disselhorst, M. C. J. M. Donckers, E. J. J. Groenen, J. Schmidt, and W. E. Moerner. Magnetic resonance of a single molecular spin. *Nature*, 363(6426):242–244, May 1993.

[13] Edlyn V. Levine, Matthew J. Turner, Pauli Kehayias, Connor A. Hart, Nicholas Langellier, Raisa Trubko, David R. Glenn, Roger R. Fu, and Ronald L. Walsworth. Principles and tech-niques of the quantum diamond microscope. *Nanophotonics*, 8(11):1945–1973, 2019.

[14] Tsunenobu Kimoto and James A. Cooper. *Fundamentals of Silicon Carbide Technology: Growth, Characterization, Devices, and Applications*. Wiley, September 2014.

[15] John David Jackson. *Classical Electrodynamics*. John Wiley & Sons, Nashville, TN, 3 edi-tion, July 1998.

[16] David J Griffiths. *Introduction to Electrodynamics*. Pearson, Upper Saddle River, NJ, 4 edition, September 2012.

[17] Bo Chen. *Introduction to NMR*, pages 1–1–1–16. AIP Publishing LLCMelville, New York, October 2020.

[18] D.A. Bromley and W. Greiner. *Quantum Mechanics: An Introduction*. Physics and Astron-omy. Springer Berlin Heidelberg, 2000.

[19] Shankar Ramamurti. *Principles of quantum mechanics*. Kluwer Academic/Plenum, Dor-drecht, Netherlands, December 1995.

[20] D.C. Giancoli. *Physics for Scientists and Engineers with Modern Physics*. Physics for Scien-tists & Engineers with Modern Physics. Pearson Education, 2008.

[21] Walther Gerlach and Otto Stern. Das magnetische moment des silberatoms. *Zeitschrift fr Physik*, 9(1):353–355, December 1922.

[22] Bogdan Povh, Klaus Rith, Christoph Scholz, and Frank Zetsche. *Particles and nuclei*. Springer, Berlin, Germany, 3 edition, August 2002.

[23] X. Fan, T. G. Myers, B. A. D. Sukra, and G. Gabrielse. Measurement of the electron magnetic moment. 2022.

[24] X. Fan, T. G. Myers, B. A. D. Sukra, and G. Gabrielse. Measurement of the electron magnetic moment. *Phys. Rev. Lett.*, 130:071801, Feb 2023.

[25] Lucjan Piela. *Singlet and Triplet States for Two Electrons*, page e133–e135. Elsevier, 2014.

[26] V. Nabokov. *THEORETICAL MODELS OF MBE*, page 111–209. Elsevier, 2002.

[27] Jeannine Grüne. *Spin States and Efficiency-Limiting Pathways in Optoelectronic Materials and Devices*. PhD thesis, 2022.

[28] W B Mims. *The linear electric field effect in paramagnetic resonance*. Oxford University Press, London, England, September 1976.

[29] Joel Davidsson, Viktor Ivády, Rickard Armiento, N T Son, Adam Gali, and Igor A Abrikosov. First principles predictions of magneto-optical data for semiconductor point defect identification: the case of divacancy defects in 4h–sic. *New Journal of Physics*, 20(2):023035, February 2018.

[30] Eric Van Oort and Max Glasbeek. Electric-field-induced modulation of spin echoes of n-v centers in diamond. *Chemical Physics Letters*, 168(6):529–532, May 1990.

[31] V. M. Acosta, C. Santori, A. Faraon, Z. Huang, K.-M. C. Fu, A. Stacey, D. A. Simpson, K. Ganesan, S. Tomljenovic-Hanic, A. D. Greentree, S. Prawer, and R. G. Beausoleil. Dynamic stabilization of the optical resonances of single nitrogen-vacancy centers in diamond. *Physical Review Letters*, 108(20), May 2012.

[32] L. C. Bassett, F. J. Heremans, C. G. Yale, B. B. Buckley, and D. D. Awschalom. Electrical tuning of single nitrogen-vacancy center optical transitions enhanced by photoinduced fields. *Physical Review Letters*, 107(26), December 2011.

[33] Gunnar Jeschke. Physical chemistry iv part 2: Electron paramagnetic resonance, 2016.

[34] Abram L. Falk, Paul V. Klimov, Bob B. Buckley, Viktor Ivády, Igor A. Abrikosov, Greg Calusine, William F. Koehl, Ádám Gali, and David D. Awschalom. Electrically and mechanically tunable electron spins in silicon carbide color centers. *Phys. Rev. Lett.*, 112:187601, May 2014.

[35] Lin Liu, Jun-Feng Wang, Xiao-Di Liu, Hai-An Xu, Jin-Ming Cui, Qiang Li, Ji-Yang Zhou, Wu-Xi Lin, Zhen-Xuan He, Wan Xu, Yu Wei, Zheng-Hao Liu, Pu Wang, Zhi-He Hao, Jun-Feng Ding,

Hai-Ou Li, Wen Liu, Hao Li, Lixing You, Jin-Shi Xu, Eugene Gregoryanz, Chuan-Feng Li, and Guang-Can Guo. Coherent control and magnetic detection of divacancy spins in silicon carbide at high pressures. *Nano Letters*, 22(24):9943–9950, 2022. PMID: 36507869.

[36] Jun-Feng Wang, Lin Liu, Xiao-Di Liu, Qiang Li, Jin-Ming Cui, Di-Fan Zhou, Ji-Yang Zhou, Yu Wei, Hai-An Xu, Wan Xu, Wu-Xi Lin, Jin-Wei Yan, Zhen-Xuan He, Zheng-Hao Liu, Zhi-He Hao, Hai-Ou Li, Wen Liu, Jin-Shi Xu, Eugene Gregoryanz, Chuan-Feng Li, and Guang-Can Guo. Magnetic detection under high pressures using designed silicon vacancy centres in silicon carbide. *Nature Materials*, 22(4):489–494, March 2023.

[37] C. R. Eddy and D. K. Gaskill. Silicon carbide as a platform for power electronics. *Science*, 324(5933):1398–1400, June 2009.

[38] J.B. Casady and R.W. Johnson. Status of silicon carbide (sic) as a wide-bandgap semiconductor for high-temperature applications: A review. *Solid-State Electronics*, 39(10):1409–1422, 1996.

[39] Matthias Niethammer, Matthias Widmann, Sang-Yun Lee, Pontus Stenberg, Olof Kordina, Takeshi Ohshima, Nguyen Tien Son, Erik Janzén, and Jörg Wrachtrup. Vector magnetometry using silicon vacancies in $4h$-sic under ambient conditions. *Phys. Rev. Appl.*, 6:034001, Sep 2016.

[40] Corey J. Cochrane, Jordana Blacksberg, Mark A. Anders, and Patrick M. Lenahan. Vectorized magnetometer for space applications using electrical readout of atomic scale defects in silicon carbide. *Scientific Reports*, 6(1), November 2016.

[41] Nguyen T. Son and Ivan G. Ivanov. Charge state control of the silicon vacancy and divacancy in silicon carbide. *Journal of Applied Physics*, 129(21), June 2021.

[42] Qin-Yue Luo, Shuang Zhao, Qi-Cheng Hu, Wei-Ke Quan, Zi-Qi Zhu, Jia-Jun Li, and Jun-Feng Wang. High sensitivity silicon carbide divacancy-based thermometer, 2023.

[43] Qiang Li, Jun-Feng Wang, Fei-Fei Yan, Ji-Yang Zhou, Han-Feng Wang, He Liu, Li-Ping Guo, Xiong Zhou, Adam Gali, Zheng-Hao Liu, Zu-Qing Wang, Kai Sun, Guo-Ping Guo, Jian-Shun Tang, Hao Li, Li-Xing You, Jin-Shi Xu, Chuan-Feng Li, and Guang-Can Guo. Room-temperature coherent manipulation of single-spin qubits in silicon carbide with a high readout contrast. *National Science Review*, 9(5):nwab122, 07 2021.

[44] Zhengzhi Jiang, Hongbing Cai, Robert Cernansky, Xiaogang Liu, and Weibo Gao. Quantum sensing of radio-frequency signal with nv centers in sic. *Science Advances*, 9(20), May 2023.

[45] A. Lohrmann, N. Iwamoto, Z. Bodrog, S. Castelletto, T. Ohshima, T. J. Karle, A. Gali, S. Prawer, J. C. McCallum, and B. C. Johnson. Single-photon emitting diode in silicon carbide. 2015.

[46] Takeshi Ohshima, Takahiro Satoh, Hannes Kraus, Georgy V Astakhov, Vladimir Dyakonov, and Pavel G Baranov. Creation of silicon vacancy in silicon carbide by proton beam writing toward quantum sensing applications. *Journal of Physics D: Applied Physics*, 51(33):333002, July 2018.

[47] D. Simin, F. Fuchs, H. Kraus, A. Sperlich, P. G. Baranov, G. V. Astakhov, and V. Dyakonov. High-precision angle-resolved magnetometry with uniaxial quantum centers in silicon carbide. *Phys. Rev. Appl.*, 4:014009, Jul 2015.

[48] Jun-Feng Wang, Qiang Li, Fei-Fei Yan, He Liu, Guo-Ping Guo, Wei-Ping Zhang, Xiong Zhou, Li-Ping Guo, Zhi-Hai Lin, Jin-Ming Cui, Xiao-Ye Xu, Jin-Shi Xu, Chuan-Feng Li, and Guang-Can Guo. On-demand generation of single silicon vacancy defects in silicon carbide. *ACS Photonics*, 6(7):1736–1743, May 2019.

[49] F. Sardi, T. Kornher, M. Widmann, R. Kolesov, F. Schiller, T. Reindl, M. Hagel, and J. Wrachtrup. Scalable production of solid-immersion lenses for quantum emitters in silicon carbide. *Applied Physics Letters*, 117(2), July 2020.

[50] S Castelletto, C T-K Lew, Wu-Xi Lin, and Jin-Shi Xu. Quantum systems in silicon carbide for sensing applications. *Reports on Progress in Physics*, 87(1):014501, dec 2023.

[51] Yiu Yung Pang Wai Kuen Leung Nan Zhao Kin On Ho, Yang Shen and Sen Yang. Diamond quantum sensors: from physics to applications on condensed matter research. *Functional Diamond*, 1(1):160–173, 2021.

[52] Gary Wolfowicz, F. Joseph Heremans, Christopher P. Anderson, Shun Kanai, Hosung Seo, Adam Gali, Giulia Galli, and David D. Awschalom. Quantum guidelines for solid-state spin defects. *Nature Reviews Materials*, 6(10):906–925, April 2021.

[53] Scott E. Crawford, Roman A. Shugayev, Hari P. Paudel, Ping Lu, Madhava Syamlal, Paul R. Ohodnicki, Benjamin Chorpening, Randall Gentry, and Yuhua Duan. Quantum sensing for energy applications: Review and perspective. *Advanced Quantum Technologies*, 4(8), June 2021.

[54] C. L. Degen, F. Reinhard, and P. Cappellaro. Quantum sensing. *Rev. Mod. Phys.*, 89:035002, Jul 2017.

[55] David P. DiVincenzo. Quantum computation. *Science*, 270(5234):255–261, October 1995.

[56] Cristian Bonato. Quantum spintronic devices, 2022.

[57] A. Csóré, I. G. Ivanov, N. T. Son, and A. Gali. Fluorescence spectrum and charge state control of divacancy qubits via illumination at elevated temperatures in $4h$ silicon carbide. *Phys. Rev. B*, 105:165108, Apr 2022.

[58] Abram L. Falk, Paul V. Klimov, Viktor Ivády, Krisztián Szász, David J. Christle, William F. Koehl, Ádám Gali, and David D. Awschalom. Optical polarization of nuclear spins in silicon carbide. 2015.

[59] Sang-Yun Lee, Matthias Niethammer, and Jörg Wrachtrup. Vector magnetometry based on $s = \frac{3}{2}$ electronic spins. *Phys. Rev. B*, 92:115201, Sep 2015.

[60] Reinhard Kirmse. N. m. atherton. principles of electron spin resonance. ellis horwood and ptr prentice hall, physical chemistry series, ellis horwood, chichester (1993). pp. 585 §127. isbn 0 13 7217625. *Magnetic Resonance in Chemistry*, 33(8):698–698, August 1995.

[61] Roland Nagy, Matthias Niethammer, Matthias Widmann, Yu-Chen Chen, Péter Udvarhelyi, Cristian Bonato, Jawad Ul Hassan, Robin Karhu, Ivan G. Ivanov, Nguyen Tien Son, Jeronimo R. Maze, Takeshi Ohshima, Ö ney O. Soykal, Ádám Gali, Sang-Yun Lee, Florian Kaiser, and Jörg Wrachtrup. High-fidelity spin and optical control of single silicon-vacancy centres in silicon carbide. *Nature Communications*, 10(1), April 2019.

[62] Matthias Niethammer, Matthias Widmann, Torsten Rendler, Naoya Morioka, Yu-Chen Chen, Rainer Stöhr, Jawad Ul Hassan, Shinobu Onoda, Takeshi Ohshima, Sang-Yun Lee, Amlan Mukherjee, Junichi Isoya, Nguyen Tien Son, and Jörg Wrachtrup. Coherent electrical readout of defect spins in silicon carbide by photo-ionization at ambient conditions. *Nature Communications*, 10(1), December 2019.

[63] F. Dolde, H. Fedder, M. W. Doherty, T. Nöbauer, F. Rempp, G. Balasubramanian, T. Wolf, F. Reinhard, L. C. L. Hollenberg, F. Jelezko, and J. Wrachtrup. Electric-field sensing using single diamond spins. *Nature Physics*, 7(6):459–463, April 2011.

[64] Abram L. Falk, Bob B. Buckley, Greg Calusine, William F. Koehl, Viatcheslav V. Dobrovitski, Alberto Politi, Christian A. Zorman, Philip X.-L. Feng, and David D. Awschalom. Polytype control of spin qubits in silicon carbide. *Nature Communications*, 4(1), May 2013.

[65] Masazumi Fujiwara and Yutaka Shikano. Diamond quantum thermometry: from foundations to applications. *Nanotechnology*, 32(48):482002, September 2021.

[66] Viktor Ivády, Tamás Simon, Jeronimo R. Maze, I. A. Abrikosov, and Adam Gali. Pressure and temperature dependence of the zero-field splitting in the ground state of nv centers in diamond: A first-principles study. *Phys. Rev. B*, 90:235205, Dec 2014.

[67] M. W. Doherty, V. M. Acosta, A. Jarmola, M. S. J. Barson, N. B. Manson, D. Budker, and L. C. L. Hollenberg. Temperature shifts of the resonances of the nv^- center in diamond. *Phys. Rev. B*, 90:041201, Jul 2014.

[68] Taras Plakhotnik, Marcus W. Doherty, Jared H. Cole, Robert Chapman, and Neil B. Manson. All-optical thermometry and thermal properties of the optically detected spin resonances of the nv– center in nanodiamond. *Nano Letters*, 14(9):4989–4996, August 2014.

[69] Cong-Cong Li, Ming Gong, Xiang-Dong Chen, Shen Li, Bo-Wen Zhao, Yang Dong, Guang-Can Guo, and Fang-Wen Sun. Temperature dependent energy gap shifts of single color center in diamond based on modified varshni equation. *Diamond and Related Materials*, 74:119–124, April 2017.

[70] Wu-Xi Lin, Fei-Fei Yan, Qiang Li, Jun-feng Wang, Zhi-He Hao, Ji-Yang Zhou, Hao Li, Li-Xing You, Jin-Shi Xu, Chuan-Feng Li, and Guang-Can Guo. Temperature dependence of divacancy spin coherence in implanted silicon carbide. *Phys. Rev. B*, 104:125305, Sep 2021.

[71] Fei-Fei Yan, Jun-Feng Wang, Qiang Li, Ze-Di Cheng, Jin-Ming Cui, Wen-Zheng Liu, Jin-Shi Xu, Chuan-Feng Li, and Guang-Can Guo. Coherent control of defect spins in silicon carbide above 550 k. *Physical Review Applied*, 10(4), October 2018.

[72] Toan Trong Tran, Blake Regan, Evgeny A. Ekimov, Zhao Mu, Yu Zhou, Wei-bo Gao, Prineha Narang, Alexander S. Solntsev, Milos Toth, Igor Aharonovich, and Carlo Bradac. Anti-stokes excitation of solid-state quantum emitters for nanoscale thermometry. *Science Advances*, 5(5), May 2019.

[73] Qixing Wang, Qi Zhang, Xiaoxu Zhao, Xin Luo, Calvin Pei Yu Wong, Junyong Wang, Dongyang Wan, T. Venkatesan, Stephen J. Pennycook, Kian Ping Loh, Goki Eda, and Andrew T. S. Wee. Photoluminescence upconversion by defects in hexagonal boron nitride. *Nano Letters*, 18(11):6898–6905, 2018. PMID: 30260651.

[74] Jun-Feng Wang, Fei-Fei Yan, Qiang Li, Zheng-Hao Liu, Jin-Ming Cui, Zhao-Di Liu, Adam Gali, Jin-Shi Xu, Chuan-Feng Li, and Guang-Can Guo. Robust coherent control of solid-state spin qubits using anti-stokes excitation. *Nature Communications*, 12(1), May 2021.

[75] John F. Barry, Jennifer M. Schloss, Erik Bauch, Matthew J. Turner, Connor A. Hart, Linh M. Pham, and Ronald L. Walsworth. Sensitivity optimization for nv-diamond magnetometry. *Rev. Mod. Phys.*, 92:015004, Mar 2020.

[76] V. A. Soltamov, C. Kasper, A. V. Poshakinskiy, A. N. Anisimov, E. N. Mokhov, A. Sperlich, S. A. Tarasenko, P. G. Baranov, G. V. Astakhov, and V. Dyakonov. Excitation and coherent control of spin qudit modes in silicon carbide at room temperature. *Nature Communications*, 10(1), April 2019.

[77] Carmem M Gilardoni, Tom Bosma, Danny van Hien, Freddie Hendriks, Björn Magnusson, Alexandre Ellison, Ivan G Ivanov, N T Son, and Caspar H van der Wal. Spin-relaxation times exceeding seconds for color centers with strong spin–orbit coupling in sic. *New Journal of Physics*, 22(10):103051, October 2020.

[78] Oscar Bulancea-Lindvall, Nguyen T. Son, Igor A. Abrikosov, and Viktor Ivády. Dipolar spin relaxation of divacancy qubits in silicon carbide. *npj Computational Materials*, 7(1), December 2021.

[79] T. Astner, P. Koller, C. M. Gilardoni, J. Hendriks, N. T. Son, I. G. Ivanov, J. U. Hassan, C. H. van der Wal, and M. Trupke. Vanadium in silicon carbide: Telecom-ready spin centres with long relaxation lifetimes and hyperfine-resolved optical transitions, 2022.

[80] F. Fuchs, B. Stender, M. Trupke, D. Simin, J. Pflaum, V. Dyakonov, and G. V. Astakhov. Engineering near-infrared single-photon emitters with optically active spins in ultrapure silicon carbide. *Nature Communications*, 6(1), July 2015.

[81] Yuzhou Wu, Fedor Jelezko, Martin B Plenio, and Tanja Weil. Diamond quantum devices in biology. *Angewandte Chemie International Edition*, 55(23):6586–6598, April 2016.

[82] Jun-Feng Wang, Jin-Ming Cui, Fei-Fei Yan, Qiang Li, Ze-Di Cheng, Zheng-Hao Liu, Zhi-Hai Lin, Jin-Shi Xu, Chuan-Feng Li, and Guang-Can Guo. Optimization of power broadening in optically detected magnetic resonance of defect spins in silicon carbide. *Phys. Rev. B*, 101:064102, Feb 2020.

[83] A. V. Poshakinskiy and G. V. Astakhov. Optically detected spin-mechanical resonance in silicon carbide membranes. *Phys. Rev. B*, 100:094104, Sep 2019.

[84] A. N. Anisimov, D. Simin, V. A. Soltamov, S. P. Lebedev, P. G. Baranov, G. V. Astakhov, and V. Dyakonov. Optical thermometry based on level anticrossing in silicon carbide. *Scientific Reports*, 6(1), September 2016.

[85] Gary Wolfowicz, Christopher P. Anderson, Andrew L. Yeats, Samuel J. Whiteley, Jens Niklas, Oleg G. Poluektov, F. Joseph Heremans, and David D. Awschalom. Optical charge state control of spin defects in 4h-sic. *Nature Communications*, 8(1), November 2017.

[86] Christopher P Anderson, Elena O Glen, Cyrus Zeledon, Alexandre Bourassa, Yu Jin, Yizhi Zhu, Christian Vorwerk, Alexander L Crook, Hiroshi Abe, Jawad Ul-Hassan, Takeshi Ohshima, Nguyen T Son, Giulia Galli, and David D Awschalom. Five-second coherence of a single spin with single-shot readout in silicon carbide. *Sci. Adv.*, 8(5):eabm5912, February 2022.

[87] H. Kraus, V. A. Soltamov, F. Fuchs, D. Simin, A. Sperlich, P. G. Baranov, G. V. Astakhov, and V. Dyakonov. Magnetic field and temperature sensing with atomic-scale spin defects in silicon carbide. *Scientific Reports*, 4(1), July 2014.

[88] John B. S. Abraham, Cameron Gutgsell, Dalibor Todorovski, Scott Sperling, Jacob E. Epstein, Brian S. Tien-Street, Timothy M. Sweeney, Jeremiah J. Wathen, Elizabeth A. Pogue, Peter G. Brereton, Tyrel M. McQueen, Wesley Frey, B. D. Clader, and Robert Osiander. Nanotesla magnetometry with the silicon vacancy in silicon carbide. *Phys. Rev. Appl.*, 15:064022, Jun 2021.

[89] Lin Liu, Jun-Feng Wang, Xiao-Di Liu, Hai-An Xu, Jin-Ming Cui, Qiang Li, Ji-Yang Zhou, Wu-Xi Lin, Zhen-Xuan He, Wan Xu, Yu Wei, Zheng-Hao Liu, Pu Wang, Zhi-He Hao, Jun-Feng Ding, Hai-Ou Li, Wen Liu, Hao Li, Lixing You, Jin-Shi Xu, Eugene Gregoryanz, Chuan-Feng Li, and Guang-Can Guo. Coherent control and magnetic detection of divacancy spins in silicon carbide at high pressures. *Nano Letters*, 22(24):9943–9950, December 2022.

[90] Yu Zhou, Junfeng Wang, Xiaoming Zhang, Ke Li, Jianming Cai, and Weibo Gao. Self-protected thermometry with infrared photons and defect spins in silicon carbide. *Phys. Rev. Appl.*, 8:044015, Oct 2017.

[91] G. Wolfowicz, S. J. Whiteley, and D. D. Awschalom. Electrometry by optical charge conversion of deep defects in 4h-sic. *Proceedings of the National Academy of Sciences*, 115(31):7879–7883, July 2018.

[92] Stefania Castelletto, Alberto Peruzzo, Cristian Bonato, Brett C. Johnson, Marina Radulaski, Haiyan Ou, Florian Kaiser, and Joerg Wrachtrup. Silicon carbide photonics bridging quantum technology. *ACS Photonics*, 9(5):1434–1457, April 2022.

[93] Shun Kanai, F. Joseph Heremans, Hosung Seo, Gary Wolfowicz, Christopher P. Anderson, Sean E. Sullivan, Mykyta Onizhuk, Giulia Galli, David D. Awschalom, and Hideo Ohno. Generalized scaling of spin qubit coherence in over 12, 000 host materials. *Proceedings of the National Academy of Sciences*, 119(15), April 2022.

[94] Ilja Fescenko, Andrey Jarmola, Igor Savukov, Pauli Kehayias, Janis Smits, Joshua Damron, Nathaniel Ristoff, Nazanin Mosavian, and Victor M. Acosta. Diamond magnetometer enhanced by ferrite flux concentrators. *Phys. Rev. Res.*, 2:023394, Jun 2020.

[95] Tianyu Xie, Zhiyuan Zhao, Xi Kong, Wenchao Ma, Mengqi Wang, Xiangyu Ye, Pei Yu, Zhiping Yang, Shaoyi Xu, Pengfei Wang, Ya Wang, Fazhan Shi, and Jiangfeng Du. Beating the standard quantum limit under ambient conditions with solid-state spins. *Science Advances*, 7(32), August 2021.

[96] Stefania Castelletto and Alberto Boretti. Silicon carbide color centers for quantum applications. *JPhys Photonics*, 2(2):022001, April 2020.

[97] Ö. O. Soykal, Pratibha Dev, and Sophia E. Economou. Silicon vacancy center in $4h$-sic: Electronic structure and spin-photon interfaces. *Phys. Rev. B*, 93:081207, Feb 2016.

[98] S. A. Tarasenko, A. V. Poshakinskiy, D. Simin, V. A. Soltamov, E. N. Mokhov, P. G. Baranov, V. Dyakonov, and G. V. Astakhov. Spin and optical properties of silicon vacancies in silicon carbide a review. *physica status solidi (b)*, 255(1), September 2017.

[99] Fei-Fei Yan, Ai-Lun Yi, Jun-Feng Wang, Qiang Li, Pei Yu, Jia-Xiang Zhang, Adam Gali, Ya Wang, Jin-Shi Xu, Xin Ou, Chuan-Feng Li, and Guang-Can Guo. Room-temperature coherent control of implanted defect spins in silicon carbide. *npj Quantum Information*, 6(1), May 2020.

[100] H. Kraus, V. A. Soltamov, D. Riedel, S. Väth, F. Fuchs, A. Sperlich, P. G. Baranov, V. Dyakonov, and G. V. Astakhov. Room-temperature quantum microwave emitters based on spin defects in silicon carbide. *Nature Physics*, 10(2):157–162, December 2013.

[101] Zhao Mu, Soroush Abbasi Zargaleh, Hans J¨urgen von Bardeleben, Johannes E. Fröch, Milad Nonahal, Hongbing Cai, Xinge Yang, Jianqun Yang, Xingji Li, Igor Aharonovich, and Weibo Gao. Coherent manipulation with resonant excitation and single emitter creation of nitrogen vacancy centers in 4h silicon carbide. *Nano Letters*, 20(8):6142–6147, July 2020.

[102] Jun-Feng Wang, Fei-Fei Yan, Qiang Li, Zheng-Hao Liu, He Liu, Guo-Ping Guo, Li-Ping Guo, Xiong Zhou, Jin-Ming Cui, Jian Wang, Zong-Quan Zhou, Xiao-Ye Xu, Jin-Shi Xu, Chuan-Feng Li, and Guang-Can Guo. Coherent control of nitrogen-vacancy center spins in silicon carbide at room temperature. *Phys. Rev. Lett.*, 124:223601, Jun 2020.

[103] Hosung Seo, Abram L Falk, Paul V Klimov, Kevin C Miao, Giulia Galli, and David D Awschalom. Quantum decoherence dynamics of divacancy spins in silicon carbide. *Nat. Commun.*, 7(1):12935, September 2016.

[104] Fei-Fei Yan, Jun-Feng Wang, Qiang Li, Ze-Di Cheng, Jin-Ming Cui, Wen-Zheng Liu, Jin-Shi Xu, Chuan-Feng Li, and Guang-Can Guo. Coherent control of defect spins in silicon carbide above 550 k. *Phys. Rev. Appl.*, 10:044042, Oct 2018.

[105] Qin-Yue Luo, Shuang Zhao, Qi-Cheng Hu, Wei-Ke Quan, Zi-Qi Zhu, Jia-Jun Li, and Jun-Feng Wang. High-sensitivity silicon carbide divacancy-based temperature sensing. *Nanoscale*, 15:8432–8436, 2023.

[106] Andrea Morello, Jarryd J. Pla, Floris A. Zwanenburg, Kok W. Chan, Kuan Y. Tan, Hans Huebl, Mikko Möttönen, Christopher D. Nugroho, Changyi Yang, Jessica A. van Donkelaar, Andrew D. C. Alves, David N. Jamieson, Christopher C. Escott, Lloyd C. L. Hollenberg, Robert G. Clark, and Andrew S. Dzurak. Single-shot readout of an electron spin in silicon. *Nature*, 467(7316):687–691, September 2010.

[107] Yu-Wei Liao, Qiang Li, Mu Yang, Zheng-Hao Liu, Fei-Fei Yan, Jun-Feng Wang, Ji-Yang Zhou, Wu-Xi Lin, Yi-Dan Tang, Jin-Shi Xu, Chuan-Feng Li, and Guang-Can Guo. Deep-learning-enhanced single-spin readout in silicon carbide at room temperature. *Phys. Rev. Appl.*, 17:034046, Mar 2022.

[108] Junfeng Wang, Fupan Feng, Jian Zhang, Jihong Chen, Zhongcheng Zheng, Liping Guo, Wenlong Zhang, Xuerui Song, Guoping Guo, Lele Fan, Chongwen Zou, Liren Lou, Wei Zhu, and Guanzhong Wang. High-sensitivity temperature sensing using an implanted single nitrogen-vacancy center array in diamond. *Phys. Rev. B*, 91:155404, Apr 2015.

[109] Wei-Ke Quan, Lin Liu, Qin-Yue Luo, Xiao-Di Liu, and Jun-Feng Wang. Fiber-coupled silicon carbide divacancy magnetometer and thermometer. *Opt. Express*, 31(10):15592–15598, May 2023.

[110] P. V. Klimov, A. L. Falk, B. B. Buckley, and D. D. Awschalom. Electrically driven spin resonance in silicon carbide color centers. *Phys. Rev. Lett.*, 112:087601, Feb 2014.

[111] Stefania Castelletto, Abdul Salam Al Atem, Faraz Ahmed Inam, Hans Jürgen von Bardeleben, Sophie Hameau, Ahmed Fahad Almutairi, Gérard Guillot, Shin-ichiro Sato, Alberto Boretti, and Jean Marie Bluet. Deterministic placement of ultra-bright near-infrared color centers in arrays of silicon carbide micropillars. *Beilstein Journal of Nanotechnology*, 10:2383–2395, December 2019.

[112] Erik R. Eisenach, John F. Barry, Michael F. O'Keeffe, Jennifer M. Schloss, Matthew H. Steinecker, Dirk R. Englund, and Danielle A. Braje. Cavity-enhanced microwave readout of a solid-state spin sensor. *Nature Communications*, 12(1), March 2021.

[113] Ji-Yang Zhou, Qiang Li, Zhi-He Hao, Wu-Xi Lin, Zhen-Xuan He, Rui-Jian Liang, Liping Guo, Hao Li, Lixing You, Jian-Shun Tang, Jin-Shi Xu, Chuan-Feng Li, and Guang-Can Guo. Plasmonic-enhanced bright single spin defects in silicon carbide membranes. *Nano Letters*, 23(10):4334–4343, May 2023.

[114] Gopalakrishnan Balasubramanian, Philipp Neumann, Daniel Twitchen, Matthew Markham, Roman Kolesov, Norikazu Mizuochi, Junichi Isoya, Jocelyn Achard, Johannes Beck, Julia Tissler, Vincent Jacques, Philip R. Hemmer, Fedor Jelezko, and Jörg Wrachtrup. Ultralong spin coherence time in isotopically engineered diamond. *Nature Materials*, 8(5):383–387, April 2009.

[115] Johann-Martin Spaeth, Jürgen R. Niklas, and Ralph H. Bartram. *Structural Analysis of Point Defects in Solids*. Springer Berlin Heidelberg, 1992.

[116] Johann-Martin Spaeth and Harald Overhof. *Point Defects in Semiconductors and Insulators: Determination of Atomic and Electronic Structure from Paramagnetic Hyperfine Interactions*. Springer Berlin Heidelberg, 2003.

[117] John A. Weil and James R. Bolton. *Electron Paramagnetic Resonance: Elementary Theory and Practical Applications*. Wiley, May 2006.

[118] J. Wrachtrup, C. von Borczyskowski, J. Bernard, M. Orrit, and R. Brown. Optical detection of magnetic resonance in a single molecule. *Nature*, 363(6426):244–245, May 1993.

[119] X.-D. Chen, C.-H. Dong, F.-W. Sun, C.-L. Zou, J.-M. Cui, Z.-F. Han, and G.-C. Guo. Temperature dependent energy level shifts of nitrogen-vacancy centers in diamond. *Applied Physics Letters*, 99(16), October 2011.

[120] P Ščajev and K Jarašiūnas. Application of a time-resolved four-wave mixing technique for the determination of thermal properties of 4h–sic crystals. *Journal of Physics D: Applied Physics*, 42(5):055413, February 2009.

[121] Toeno van der Sar. Magnetometry with spins in diamond. Measuring a magnetic field with NV spins. Measuring a magnetic field with NV spins - Magnetometry with spins in diamond. (n.d.). `https://magnetometryrp.quantumtinkerer.tudelft.nl/3_NVspin/`. [Accessed 05-08-2024].

[122] C. L. Degen. Scanning magnetic field microscope with a diamond single-spin sensor. *Applied Physics Letters*, 92(24):243111, June 2008.

[123] Linh Pham, Nir Bar-Gill, David Le Sage, A. Stacey, M. Markham, Daniel Twitchen, M. Lukin, and R. Walsworth. Enhanced metrology using preferential orientation of nitrogen-vacancy centers in diamond. *Physical Review B*, 86, 07 2012.

[124] Sang-Yun Lee, Matthias Niethammer, and Jörg Wrachtrup. Vector magnetometry based on s=3/2 electronic spins. 2015.

[125] Gopalakrishnan Balasubramanian, I. Y. Chan, Roman Kolesov, Mohannad Al-Hmoud, Julia Tisler, Chang Shin, Changdong Kim, Aleksander Wojcik, Philip R. Hemmer, Anke Krueger, Tobias Hanke, Alfred Leitenstorfer, Rudolf Bratschitsch, Fedor Jelezko, and Jörg Wrachtrup. Nanoscale imaging magnetometry with diamond spins under ambient conditions. *Nature*, 455(7213):648–651, October 2008.

[126] Erik Janzén, Adam Gali, Patrick Carlsson, Andreas Gällstr öm, Björn Magnusson, and N.T. Son. The silicon vacancy in sic. *Physica B: Condensed Matter*, 404(22):4354–4358, December 2009.

[127] J. Isoya, T. Umeda, N. Mizuochi, N. T. Son, E. Janzén, and T. Ohshima. Epr identification of intrinsic defects in sic. *physica status solidi (b)*, 245(7):1298–1314, June 2008.

[128] Lawrence J Berliner and Jacques Reuben, editors. *Spin labeling*. Biological magnetic resonance. Springer, New York, NY, September 2011.

[129] Pavel Baranov Baranov, Hans Jurgen Von Bardeleben, Fedor Jelezko, and Jorg Wrachtrup. *Magnetic resonance of semiconductors and their nanostructures*. Springer series in materials science. Springer, Vienna, Austria, 1 edition, March 2017.

[130] Peter W Atkins and Ronald S Friedman. *Molecular Quantum Mechanics*. Oxford University Press, London, England, 5 edition, November 2010.

[131] P. V. Klimov, A. L. Falk, B. B. Buckley, and D. D. Awschalom. Electrically driven spin resonance in silicon carbide color centers. *Physical Review Letters*, 112(8), February 2014.

[132] Felix M. Stürner, Andreas Brenneis, Thomas Buck, Julian Kassel, Robert Rölver, Tino Fuchs, Anton Savitsky, Dieter Suter, Jens Grimmel, Stefan Hengesbach, Michael Förtsch, Kazuo Nakamura, Hitoshi Sumiya, Shinobu Onoda, Junichi Isoya, and Fedor Jelezko. Integrated and portable magnetometer based on nitrogen-vacancy ensembles in diamond. *Advanced Quantum Technologies*, 4(4), February 2021.

[133] *Electron Paramagnetic Resonance: A Practitioner's Toolkit*. Wiley, July 2008.

[134] Daniella Goldfarb and Stefan Stoll, editors. *EPR spectroscopy*. eMagRes Books. Standards Information Network, March 2018.

[135] Sabine Richert, Claudia E. Tait, and Christiane R. Timmel. Delocalisation of photoexcited triplet states probed by transient epr and hyperfine spectroscopy. *Journal of Magnetic Resonance*, 280:103–116, July 2017.

[136] Gabriele Rainò, Nuri Yazdani, Simon C. Boehme, Manuel Kober-Czerny, Chenglian Zhu, Franziska Krieg, Marta D. Rossell, Rolf Erni, Vanessa Wood, Ivan Infante, and Maksym V. Kovalenko. Ultra-narrow room-temperature emission from single cspbbr3 perovskite quantum dots. *Nature Communications*, 13(1), May 2022.

[137] M. S. J Barson, L. M. Oberg, L. P. McGuinness, A. Denisenko, N. B. Manson, J. Wrachtrup, and M. W. Doherty. Nanoscale vector electric field imaging using a single electron spin. 2020.

[138] Qiang Li, Jun-Feng Wang, Fei-Fei Yan, Ji-Yang Zhou, Han-Feng Wang, He Liu, Li-Ping Guo, Xiong Zhou, Adam Gali, Zheng-Hao Liu, Zu-Qing Wang, Kai Sun, Guo-Ping Guo, Jian-Shun Tang, Hao Li, Li-Xing You, Jin-Shi Xu, Chuan-Feng Li, and Guang-Can Guo. Room-temperature coherent manipulation of single-spin qubits in silicon carbide with a high readout contrast. *National Science Review*, 9(5), July 2021.

[139] Qin-Yue Luo, Qiang Li, Jun-Feng Wang, Pei-Jie Guo, Wu-Xi Lin, Shuang Zhao, Qi-Cheng Hu, Zi-Qi Zhu, Jin-Shi Xu, Chuan-Feng Li, and Guang-Can Guo. Fabrication and quantum sensing of spin defects in silicon carbide. *Frontiers in Physics*, 11, September 2023.